Monthly Notices
of the
ROYAL ASTRONOMICAL SOCIETY

MNRAS **497,** 609–625 (2020)
Advance Access publication 2020 July 7

doi:10.1093/mnras/staa1979

Chemical models of interstellar cyanomethanimine isomers

Xia Zhang [1,2] Donghui Quan,[1,3]★ Qiang Chang,[1,4] Eric Herbst,[5] Jarken Esimbek[1,6] and Matthew Webb[3]

[1]*Xinjiang Astronomical Observatory, Chinese Academy of Sciences, 150 Science 1-Street, Urumqi, Xinjiang 830011, China*
[2]*University of the Chinese Academy of Sciences, Beijing 100049, China*
[3]*Department of Chemistry, Eastern Kentucky University, Richmond, KY 40475, USA*
[4]*School of Physics and Optoelectronic Engineering, Shandong University of Technology, Zibo 255000, China*
[5]*Departments of Chemistry and Astronomy, University of Virginia, Charlottesville, VA 22904, USA*
[6]*Key Laboratory of Radio Astronomy, Chinese Academy of Sciences, Urumqi 830011, China*

Accepted 2020 June 30. Received 2020 June 6; in original form 2020 February 3

ABSTRACT

The E-isomer of cyanomethanimine (HNCHCN) was first identified in Sagittarius B2(N) (Sgr B2(N)) by a comparison of the publicly available Green Bank Telescope (GBT) PRIMOS survey with laboratory rotational spectra. Recently, Z-cyanomethanimine was detected in the quiescent molecular cloud G+0.693−0.027 with the IRAM 30-m telescope. Cyanomethanimine is a chemical intermediate in the proposed synthetic routes of adenine, and may play an important role in forming biological molecules in the interstellar medium. Here we present a new modelling study of cyanomethanimine, using the NAUTILUS gas–grain reaction network and code with the addition of over 400 chemical reactions of the three cyanomethanimine isomers and related species. We apply cold isothermal core, hot core, and C-type shock models to simulate the complicated and heterogeneous physical environment in and in front of Sgr B2(N), and in G+0.693−0.027. We identify the major formation and destruction routes of cyanomethanimine, and find that the calculated abundances of the cyanomethanimine isomers and the ratio of Z-isomer to E-isomer are both in reasonable agreement with observations for selected environments. In particular, we conclude that these isomers are most likely formed within or near the hot core without the impact of shocks, or in the cold regions with shocks.

Key words: astrochemistry – shock waves – ISM: abundances – ISM: molecules.

1 INTRODUCTION

Complex organic molecules (COMs) represent a major topic in the field of astrochemistry and astrobiology. Unlike the unsaturated and exotic molecular species known as carbon chains, COMs are often representative of terrestrial organic chemistry. Some of these molecules can serve as precursors of biological molecules, and are thus labelled prebiotic molecules. Cyanomethanimine (HNCHCN), the COM studied here, can possibly be a precursor of adenine, the pentamer of HCN, and a purine of DNA and RNA nucleobases. It has been suggested that the route to adenine occurs via neutral–neutral reactions (Chakrabarti & Chakrabarti 2000; Smith, Talbi & Herbst 2001). Interestingly, the pathway from HCN to adenine seems to be inefficient under interstellar medium (ISM) conditions (Smith et al. 2001), making adenine's possible synthesis from cyanomethanimine the more important. Cyanomethanimine is one of the products of the photoreactivity of aminoacetonitrile (CH_2NH_2CN, AAN; Borget et al. 2012). In astrophysical environments, AAN is viewed as a precursor of glycine, the smallest amino acid molecule (Brown et al. 1977; Belloche et al. 2008), and AAN has been detected in the direction of Sagittarius B2 (Sgr B2; Belloche et al. 2008).

Cyanomethanimine has three isomers, labelled Z, E, and N, and can be regarded as a dimer of HCN. It is lower in energy than the separated HCN monomers, although the potential pathway between the dimer and the monomers has a significant barrier (Smith et al. 2001). Among the isomers, Z- and E-cyanomethanimine are significantly lower in energy than the N-isomer, and are thought to be closely spaced in energy with structures that depend upon whether the two hydrogen atoms are cis or trans to each other (Clemmons 1983; Winnewisser, Winnewisser & Wentrup 1984; Takano et al. 1990; Smith et al. 2001). E-cyanomethanimine was detected towards the massive star-forming region Sgr B2(N) by comparison of laboratory data with spectra from the Green Bank Telescope (GBT) PRIMOS data by Zaleski et al. (2013). The column density of E-cyanomethanimine was derived to be approximately$1.5(2) \times 10^{13}$ cm^{-2}. Although the amount of Z-cyanomethanimine is similar to that of E-cyanomethanimine in experiments, and it is even slightly lower in energy, the intensity of rotational transitions of Z-cyanomethanimine is significantly weaker because of the difference in dipole moment components (Zaleski et al. 2013), making it more difficult to detect. Searches by Melosso et al. (2018) for both isomers in low-mass star-forming regions were unsuccessful, with derived upper limits for the abundances of the E- and Z-isomers of a few $\times 10^{-10}$ for starless cores and hot corinos, and a less rigorous upper limit, $\leq 10^{-9}$, for shocked regions. Recently, Rivilla et al. (2019) reported the first detection of Z-cyanomethanimine along with some transitions of the E-isomer in the quiescent molecular cloud G+0.693−0.027 (G+0.693 hereafter) with the IRAM 30-m telescope, and obtained a column density for Z-cyanomethanimine of $2.0(0.6) \times 10^{14}$ cm^{-2}. Their results suggest temperatures in excess of 100 K. A significant number of such clouds, known as Galactic Centre (GC) clouds, have been studied and appear to have similar chemistry to hot cores, with high abundances of

★ E-mail: quandh@xao.ac.cn

Table 1. The column densities of E-, Z-cyanomethanimine and molecular hydrogen towards different types of sources.

Source name	N(Z-isomer) (cm^{-2})	N(E-isomer) (cm^{-2})	N(H$_2$) (cm^{-2})
Sgr B2(N)	–	5.0×10^{13} [a]	4.0×10^{23} [b], 1.54×10^{25} [c]
Molecular cloud G+0.693	2.0×10^{14} [d]	3.3×10^{13} [d]	1.35×10^{23} [e]
Starless core L1544	$\leq 1 \times 10^{11}$ [f]	$\leq 1 \times 10^{11}$ [f]	$\simeq 10^{23}$ [g]
L1577-B1	$\leq 1 \times 10^{12}$ [f]	$\leq 1 \times 10^{12}$ [f]	$\simeq 10^{21}$ [h]
SVS13-A and IRAS4A	$\leq 3 \times 10^{12}$ [f]	$\leq 3 \times 10^{12}$ [f]	$\simeq 10^{24}$ [i]

[a]Vazart et al. (2015a); [b]Quan et al. (2016); [c]Bonfand et al. (2017); [d]Rivilla et al. (2019); [e]Martín et al. (2008); [f](upper limit values) Melosso et al. (2018); [g]Crapsi et al. (2005); [h]Lefloch et al. (2012); [i]Looney, Mundy & Welch (2000) and Maret et al. (2002).

COMs, but with some differences that are partially due to the lack of central protostars to cause desorption (Requena-Torres et al. 2006). These observational results are summarized in Table 1.

The line of sight towards Sgr B2 contains diverse interstellar matter, including hot-core material (100–300 K), GC clouds, cooler material in front of the hot cores, and translucent material lying at significant distance from Sgr B2 such as in spiral arms and dynamically independent from Sgr B2. E-cyanomethanimine is one of a number of larger molecules identified towards Sgr B2(N) that have been found to have low rotational temperatures ($\sim$10 K), and are either subthermal due to low density or formed in dense cold conditions. Our knowledge of how COMs form under each of these diverse physical conditions is mixed. Detailed simulations involving mainly grain chemistry are able to explain the molecules detected in hot cores surrounding protostars and young stars as being formed during thermal warm-up mainly on grains and subsequently desorbed into the gas at even higher temperatures (Garrod, Widicus Weaver & Herbst 2008). The formation of COMs in cold dense sources is not understood as well, with explanations involving a number of exotic reaction mechanisms on grains followed by non-thermal desorption and neutral–neutral gas-phase chemistry (Balucani, Ceccarelli & Taquet 2015; Chuang et al. 2015). Molecules detected at higher temperatures in the GC clouds have long been considered to form on grains but the absence of nearby protostars leads to the suggestion of desorption by shocks. Shocks with moderate velocities of $\sim$10 km s^{-1} are required to sputter molecules from the icy mantles on grains (Draine & Salpeter 1979; Martín-Pintado et al. 1999; Requena-Torres et al. 2006). The formation of COMs in diffuse or translucent material remains at least partially a mystery to the best of our knowledge, with suggestions such as cycling of material between dense and diffuse stages, and small nuggets of dense material located within the translucent gas.

In an attempt to reproduce the observed abundances and upper limits for the Z- and E-isomers of cyanomethanimine towards the GC and other sources, we have considered several different physical environments and, with the addition of formation and destruction reactions of cyanomethanimine and related species, run chemical simulations to calculate its abundance. In Section 2, we present the chemistry of cyanomethanimine and related species. This is followed in Section 3 with a description of the chemical models and assorted physical conditions. The results are described in Section 4 and our findings are summarized in Section 5.

2 FORMATION AND DESTRUCTION OF THE CYANOMETHANIMINE ISOMERS

The chemistry of the formation and destruction of the cyanomethanimine isomers has been looked at by a number of investigators. Chakrabarti & Chakrabarti (2000) proposed that cyanomethanimine can be formed by the dimerization of two HCN molecules, but as already noted, the barrier for this process is considerable (Smith et al. 2001; Yim & Choe 2012). Another pathway, proposed by Yim & Choe (2012) and Jung & Choe (2013), followed the dimerization of the protonated species. The reaction barrier for dimerization of HCN or HNC could be lower with the aid of protons. Moreover HCN or HNC can possibly react with HCNH$^+$. However, Yim & Choe (2012) suggested that this process cannot produce cyanomethanimine efficiently under interstellar conditions.

Using electronic structure theory and kinetic calculations and second-order vibrational perturbation theory, Vazart et al. (2015a,b) proposed the gas-phase reactions between CN and methanimine (CH$_2$NH) to produce all three isomers of cyanomethanimine,

$$\mathrm{CN + CH_2NH \rightarrow Z\text{-}HNCHCN + H}, \quad (1)$$

$$\mathrm{CN + CH_2NH \rightarrow E\text{-}HNCHCN + H}, \quad (2)$$

$$\mathrm{CN + CH_2NH \rightarrow N\text{-}CH_2NCN + H}, \quad (3)$$

and calculated rate coefficients for all three processes. At 10 K, the calculated rate coefficients are 2.7×10^{-10}, 1.9×10^{-10}, and 1.6×10^{-11} cm^3 s^{-1}, respectively. The large values are partially due to tunnelling processes. These reactions also can occur on the surface of dust particles where the two reactant molecules are adsorbed on the surface, meet and bond each other, and then form new molecules according to the Langmuir–Hinshelwood formation mechanism (Hasegawa, Herbst & Leung 1992). Because of the importance of CN and CH$_2$NH molecules as reactants, we also consider the reaction of CN + H$_2$O $\rightarrow$ HNCOH on the grain surface. As Rimola et al. (2018) concluded that CN radicals readily react with the water molecules once they start interacting with the ice, we added related reactions to the reaction network, and show them with other reactions not involving cyanomethanimine online (supplemental tables). Besides, the reactants CN and CH$_2$NH may significantly be converted to HCN and CH$_3$NH$_2$ on the grain surface through a set of hydrogenation processes (Theule et al. 2011). These reactions are all included in this study.

Reactions (4) and (5), which possess the same intermediate (CNCH$_2$NH) as reactions (1) and (2), likely have similar formation routes that lead to cyanomethanimine:

$$\mathrm{NH + H_2CCN \rightarrow Z\text{-}HNCHCN + H}, \quad (4)$$

$$\mathrm{NH + H_2CCN \rightarrow E\text{-}HNCHCN + H}. \quad (5)$$

They have also been incorporated into our models to produce cyanomethanimine. The surface analogues of these processes are also included. Throughout the remainder of the paper, surface species are designated by the initial letter J.

In addition, the following radical–radical reactions, can likely occur on the surface of dust particles and are assumed to be barrierless except for diffusion, although studies show that these reactions might have a barrier once the radicals attach to water ice (Enrique-Romero et al. 2019):

$$\mathrm{JNH} + \mathrm{JHCCN} \rightarrow \mathrm{JZ\text{-}HNCHCN}, \quad (6)$$

$$\mathrm{JNH} + \mathrm{JHCCN} \rightarrow \mathrm{JE\text{-}HNCHCN}, \quad (7)$$

$$\mathrm{JCN} + \mathrm{JHCNH} \rightarrow \mathrm{JZ\text{-}HNCHCN}, \quad (8)$$

$$\mathrm{JCN} + \mathrm{JHCNH} \rightarrow \mathrm{JE\text{-}HNCHCN}, \quad (9)$$

$$\mathrm{JCN} + \mathrm{JH_2CN} \rightarrow \mathrm{JN\text{-}CH_2NCN}. \quad (10)$$

These radical–radical reactions are probably slow in the gas because they can only occur by the emission of a photon. JH_2CN and JHCCN are formed by the reactions of JCH_2 + JN and JCH + JCN, JCCN + JH on grain surface (Hasegawa et al. 1992; Garrod, Wakelam & Herbst 2007; Hassel, Herbst & Garrod 2008; Quan et al. 2010; Wakelam et al. 2015).

For the Z-, E-, and N-isomers, we determine their binding (desorption) energies E_D to the grain surface by adding their constituent parts, i.e. $E_D = E_D(\mathrm{CN}) + E_D(\mathrm{CHNH})$, and assume that all three isomers have the same binding energies. The binding energies of other species in the network are from the gas–grain code NAUTILUS (Reboussin et al. 2014; Ruaud, Wakelam & Hersant 2016). Although the potential barriers (activation energy) of surface reactions (6)–(10) are zero, the reaction rate coefficients are too small at low temperature to be of any importance, due to the large diffusive barriers of reactants. The reactions play a more important role in cyanomethanimine formation at higher temperatures. Once formed, the gaseous cyanomethanimine isomers can be destroyed by reactions with positive ions, as well as cosmic ray induced and external ultraviolet (UV) caused photodissociation. There is a high isomerization barrier (≈26.5 kcal $\mathrm{mol^{-1}}$) calculated between the E- and Z-isomers (Puzzarini 2015). The isomerization barriers between the E-/Z- and N-isomers are likely to be even higher based on their highly different molecular structures. Therefore the isomerization reactions have been neglected.

Rate coefficients for the additional reactions involving the chemistry of the cyanomethanimine isomers, using the E-isomer as an example, are summarized in Table 2, for gas-phase processes, and Table 3, for surface processes. The rate coefficients in Table 2 are defined in terms of three parameters α, β, and γ through the equation

$$k(T) = \alpha \times (T(\mathrm{K})/300)^{\beta} \times \exp(-\gamma/T(\mathrm{K})), \quad (11)$$

where the parameters depend upon the type of process. Specific values are given for a temperature of 10 K. For neutral–neutral reactions and dissociative recombination, α and the overall rate coefficient k are in units of $\mathrm{cm^3\ s^{-1}}$, whereas for (external UV) photodissociation, α and k are in units of $\mathrm{s^{-1}}$ while the parameter γ multiplies the negative of the visual extinction. For cosmic ray-induced photodissociation, α is the product of a unitless number in the table multiplied by the cosmic ray ionization ζ, which is normally assumed to be in the vicinity of 1.3×10^{-17} $\mathrm{s^{-1}}$ and k is in units of $\mathrm{s^{-1}}$. The parameters in equation (11) are quoted from similar reactions suggested in Vazart et al. (2015a) and Quan et al. (2016). Finally, for cation–neutral reactions with a dipolar neutral reactant, the parameter α is the unitless branching fraction of the products, the parameter β is the so-called Langevin rate coefficient in units of $\mathrm{cm^3\ s^{-1}}$, and the parameter γ multiplies β to yield the total rate coefficient at 10 K (Woon & Herbst 2009).

For surface reactions listed in Table 3, the rate coefficients for the photodissociation processes are handled in the same manner as for gas-phase species, while thermal desorption is treated using the first-order Polanyi–Wigner equation with a trial frequency of the ith species,

$$\nu_i = \sqrt{\frac{2N_s k_B E_{des}}{\pi^2 m m_p}}, \quad (12)$$

in units of $\mathrm{s^{-1}}$ (Semenov et al. 2010). In the equation, N_s is the number density of surface sites per grain ($\mathrm{cm^{-2}}$), k_B is the Boltzmann constant (erg $\mathrm{K^{-1}}$), E_{des} is the desorption energy (K) of species, m is the mass of the species (g), and m_p is the proton mass (g). The rate coefficient for accretion per dust particle with a radius of 0.1 μm is given in terms of the granular cross-section σ ($\mathrm{cm^2}$) and the thermal velocity v_{th} of the adsorbing particle ($\mathrm{cm\ s^{-1}}$).

Regarding surface reactions that proceed via diffusion, the rate coefficient is a product of several factors. For each reactant, its trial frequency is multiplied by the efficiency of hopping from one potential well over a diffusion barrier, assumed to be 0.5 of the desorption energy, to an adjacent potential well. This product is then divided by the number of potential wells per grain to get a diffusion rate over the whole grain. Reaction occurs when two species are found in the same potential well. If the reaction possesses a chemical activation energy, however, it is necessary to include another factor, which we term the probability P for tunnelling under this barrier. This probability is calculated from the formula

$$P = \alpha \exp[-2(b/\hbar)(2k_B \mu(i) m_p E_a)^{1/2}] \quad (13)$$

(Hasegawa et al. 1992), where b is the barrier thickness (1 Å), $\mu(i)$ is the reduced mass of the reactants, and E_a is the activation energy of reaction (K). The reactions involving Z-, N-isomers and related species are listed online (Tables A1–A6 as supplementary material).

2.1 Quantum chemical calculations

All new quantum chemical calculations reported here were undertaken by using the hybrid density function B3LYP method (Lee, Yang & Parr 1988; Becke 1993), in conjunction with the 6-311G(d, p) basis set to obtain the molecular structures. The higher level aug-cc-pVTZ method was used to evaluate the relative energies of all species. Zero-point vibrational energies were calculated to correct the energies. For cation–neutral reactions, we used quantum chemical calculations to optimize molecular structures, and to compute the dipole moment and the dipole polarizability for the neutral species. Then we used the Langevin expression and the Su–Chesnavich formulae to calculate the rate coefficients at 10 K (Woon & Herbst 2009). The QST2 method was adopted to get closer to the quadratic region around the transition state for neutral–neutral molecular reactions to form cyanomethanimine (Peng & Schlegel 1993). All quantum chemical calculations were run with the GAUSSIAN 09 program package (Frisch et al. 2009).

3 CHEMICAL MODEL

3.1 The gas–grain code

We use the two-phase gas–grain version of NAUTILUS, which includes both the gas-phase and dust grain surface chemistry. It calculates abundances of gas-phase and grain-surface species with respect

Table 2. Summary of the rate coefficients of gas-phase reactions involving E-cyanomethanimine.

Reaction	α	β	γ	k (10 K)	Ref.
Cosmic ray-induced photodissociation	(–)	(–)	(–)	(s^{-1})	
E-HNCHCN → HCN + HNC	1.50E + 03	0	0	1.95E-14	*a*
E-HNCHCN → HCNH + CN	1.50E + 03	0	0	1.95E-14	*a*
E-HNCHCN → NCHCN + H	1.50E + 03	0	0	1.95E-14	*a*
E-HNCHCN → HNCCN + H	1.50E + 03	0	0	1.95E-14	*a*
HNCCN → HNC + CN	1.50E + 03	0	0	1.95E-14	*a*
HNCCN → NCCN + H	1.50E + 03	0	0	1.95E-14	*a*
NCHCN → HCN + CN	1.50E + 03	0	0	1.95E-14	*a*
NCHCN → NCCN + H	1.50E + 03	0	0	1.95E-14	*a*
NCCN → CN + CN	1.50E + 03	0	0	1.95E-14	*a*
HCNH → CH + NH	1.50E + 03	0	0	1.95E-14	*a*
HCNH → HCN + H	1.50E + 03	0	0	1.95E-14	*a*
HCNH → HNC + H	1.50E + 03	0	0	1.95E-14	*a*
Photodissociation	(s^{-1})	(–)	(–)	(s^{-1})	
E-HNCHCN → HCN + HNC	1.00E-09	0	1.9	5.60E-18	*a*
E-HNCHCN → HCNH + CN	1.00E-09	0	1.9	5.60E-18	*a*
E-HNCHCN → NCHCN + H	1.00E-09	0	1.9	5.60E-18	*a*
E-HNCHCN → HNCCN + H	1.00E-09	0	1.9	5.60E-18	*a*
HNCCN → HNC + CN	1.00E-09	0	1.9	5.60E-18	*a*
HNCCN → NCCN + H	1.00E-09	0	1.9	5.60E-18	*a*
NCHCN → HCN + CN	1.00E-09	0	1.9	5.60E-18	*a*
NCHCN → NCCN + H	1.00E-09	0	1.9	5.60E-18	*a*
NCCN → CN + CN	1.00E-09	0	1.9	5.60E-18	*a*
HCNH → CH + NH	1.00E-09	0	1.9	5.60E-18	*a*
HCNH → HCN + H	1.00E-09	0	1.9	5.60E-18	*a*
HCNH → HNC + H	1.00E-09	0	1.9	5.60E-18	*a*
Cation–neutral	(–)	($cm^3\ s^{-1}$)	(–)	($cm^3\ s^{-1}$)	
C^+ + E-HNCHCN → $HNCHCN^+$ + C	0.25	1.77E-09	6.09	7.31E-09	*b*
C^+ + E-HNCHCN → C_2N^+ + HCNH	0.25	1.77E-09	6.09	7.31E-09	*b*
C^+ + E-HNCHCN → HC_2N^+ + HCN	0.25	1.77E-09	6.09	7.31E-09	*b*
C^+ + E-HNCHCN → HC_2N^+ + HNC	0.25	1.77E-09	6.09	7.31E-09	*b*
H^+ + E-HNCHCN → H_2CN^+ + HNC	0.35	5.59E-09	6.09	3.24E-08	*b*
H^+ + E-HNCHCN → HCNH + HCN^+	0.35	5.59E-09	6.09	3.24E-08	*b*
H^+ + E-HNCHCN → $HNCHCN^+$ + H	0.30	5.59E-09	6.09	2.77E-08	*b*
He^+ + E-HNCHCN → $HCNH^+$ + CN + He	0.25	2.87E-09	6.09	1.19E-08	*b*
He^+ + E-HNCHCN → HCNH + CN^+ + He	0.25	2.87E-09	6.09	1.19E-08	*b*
He^+ + E-HNCHCN → HCN + HNC^+ + He	0.25	2.87E-09	6.09	1.19E-08	*b*
He^+ + E-HNCHCN → HCN^+ + HNC + He	0.25	2.87E-09	6.09	1.19E-08	*b*
H_3^+ + E-HNCHCN → HCN^+ + HCNH + H_2	0.50	3.29E-09	6.09	2.72E-08	*b*
H_3^+ + E-HNCHCN → $HNCHCNH^+$ + H_2	0.50	3.29E-09	6.09	2.72E-08	*b*
H_3O^+ + E-HNCHCN → HCN^+ + HCNH + H_2O	0.50	1.48E-09	6.09	1.22E-08	*b*
H_3O^+ + E-HNCHCN → $HNCHCNH^+$ + H_2O	0.50	1.48E-09	6.09	1.22E-08	*b*
HCO^+ + E-HNCHCN → HCN^+ + HCNH + CO	0.50	1.28E-09	6.09	1.05E-08	*b*
HCO^+ + E-HNCHCN → $HNCHCNH^+$ + CO	0.50	1.28E-09	6.09	1.05E-09	*b*
$HCNH^+$ + HCN → $HNCHCN^+$ + H	1	1.00E-09	6.63	1.80E-08	*b*
$HCNH^+$ + HNC → $HNCHCN^+$ + H	1	1.04E-09	6.43	1.82E-08	*b*
C^+ + NCHCN → $NCHCN^+$ + C	1	1.70E-09	4.04	1.90E-08	*b*
H^+ + NCHCN → $NCHCN^+$ + H	0.30	5.37E-09	4.04	1.80E-08	*b*
H^+ + NCHCN → $HCNH^+$ + CN	0.35	5.37E-09	4.04	2.10E-08	*b*
H^+ + NCHCN → HCN^+ + HCN	0.35	5.37E-09	4.04	2.10E-08	*b*
He^+ + NCHCN → HCN^+ + CN + He	0.50	2.76E-09	4.04	1.54E-08	*b*
He^+ + NCHCN → HCN + CN^+ + He	0.50	2.76E-09	4.04	1.54E-08	*b*
H_3^+ + NCHCN → $HNCHCN^+$ + H_2	0.30	3.16E-09	4.04	1.06E-08	*b*
H_3^+ + NCHCN → $HCNH^+$ + CN + H_2	0.35	3.16E-09	4.04	1.23E-08	*b*
H_3^+ + NCHCN → HCN + HCN^+ + H_2	0.35	3.16E-09	4.04	1.23E-08	*b*
H_3O^+ + NCHCN → HCN^+ + HCN + H_2O	0.35	1.42E-09	4.04	5.56E-09	*b*
H_3O^+ + NCHCN → $HCNH^+$ + CN + H_2O	0.35	1.42E-09	4.04	5.56E-09	*b*
H_3O^+ + NCHCN → $HNCHCN^+$ + H_2O	0.30	1.42E-09	4.04	4.77E-09	*b*
HCO^+ + NCHCN → HCN + HCN^+ + CO	0.35	1.23E-09	4.04	4.80E-09	*b*
HCO^+ + NCHCN → $HCNH^+$ + CN + CO	0.35	1.23E-09	4.04	4.80E-09	*b*
HCO^+ + NCHCN → $HNCHCN^+$ + CO	0.30	1.23E-09	4.04	4.12E-09	*b*
C^+ + HNCCN → $HNCCN^+$ + C	1	1.81E-09	4.97	2.47E-08	*b*
H^+ + HNCCN → $HNCCN^+$ + H	0.30	5.73E-09	4.97	2.34E-08	*b*

Table 2 – *continued*

Reaction	α	β	γ	k (10 K)	Ref.
$H^+ + HNCCN \rightarrow HCN^+ + HNC$	0.35	5.73E-09	4.97	2.73E-08	b
$H^+ + HNCCN \rightarrow HCNH^+ + CN$	0.35	5.73E-09	4.97	2.73E-08	b
$He^+ + HNCCN \rightarrow HNC^+ + CN + He$	0.50	2.94E-09	4.97	2.00E-08	b
$He^+ + HNCCN \rightarrow HNC + CN^+ + He$	0.50	2.94E-09	4.97	2.00E-08	b
$H_3^+ + HNCCN \rightarrow HNCHCN^+ + H_2$	0.30	3.37E-09	4.97	1.37E-08	b
$H_3^+ + HNCCN \rightarrow HNC + HCN^+ + H_2$	0.35	3.37E-09	4.97	1.60E-08	b
$H_3^+ + HNCCN \rightarrow HCNH^+ + CN + H_2$	0.35	3.37E-09	4.97	1.60E-08	b
$H_3O^+ + HNCCN \rightarrow HCN^+ + HNC + H_2O$	0.35	1.52E-09	4.97	7.22E-09	b
$H_3O^+ + HNCCN \rightarrow HCNH^+ + CN + H_2O$	0.35	1.52E-09	4.97	7.22E-09	b
$H_3O^+ + HNCCN \rightarrow HNCHCN^+ + H_2O$	0.30	1.52E-09	4.97	6.19E-09	b
$HCO^+ + HNCCN \rightarrow HNC + HCN^+ + CO$	0.35	1.31E-09	4.97	6.24E-09	b
$HCO^+ + HNCCN \rightarrow HCNH^+ + CN + CO$	0.35	1.31E-09	4.97	6.24E-09	b
$HCO^+ + HNCCN \rightarrow HNCHCN^+ + CO$	0.30	1.31E-09	4.97	5.35E-09	b
$C^+ + NCCN \rightarrow CNC^+ + CN$	1.00E-09	0.00	0.00	1.00E-09	c
$H^+ + NCCN \rightarrow NCCN^+ + H$	4.00E-09	0.00	0.00	1.00E-09	c
$He^+ + NCCN \rightarrow CN^+ + CN + He$	8.00E-10	0.00	0.00	8.00E-10	d
$He^+ + NCCN \rightarrow C_2N^+ + N + He$	8.00E-10	0.00	0.00	8.00E-10	d
$H_3^+ + NCCN \rightarrow HNCCN^+ + H_2$	2.80E-09	0.00	0.00	2.80E-09	e
$H_3O^+ + NCCN \rightarrow HCN^+ + CN + H_2O$	0.25	1.40E-09	0.00	3.50E-10	b
$H_3O^+ + NCCN \rightarrow HNC^+ + CN + H_2O$	0.25	1.40E-09	0.00	3.50E-10	b
$H_3O^+ + NCCN \rightarrow HNCCN^+ + H_2O$	0.25	1.40E-09	0.00	3.50E-10	b
$H_3O^+ + NCCN \rightarrow NCHCN^+ + H_2O$	0.25	1.40E-09	0.00	3.50E-10	b
$HCO^+ + NCCN \rightarrow HNCCN^+ + CO$	1.70E-09	0.00	0.00	1.70E-09	c
Neutral–neutral	(cm^3 s^{-1})	(–)	(–)	(cm^3 s^{-1})	
$CN + CH_2NH \rightarrow E\text{-}HNCHCN + H$	3.15E-10	0.152	9.05E-02	1.86E-10	f, g
$NH + H_2CCN \rightarrow E\text{-}HNCHCN + H$	3.15E-10	0.152	9.05E-02	1.86E-10	f, g
$CH + NCCN \rightarrow CCN + HCN$	2.00E-10	0.00	0.00	2.00E-10	c
$CN + HNC \rightarrow NCCN + H$	2.00E-10	0.00	0.00	2.00E-10	h
$N + C_3N \rightarrow C + NCCN$	6.00E-11	0.00	0.00	6.00E-11	c
Dissociative recombination	(cm^3 s^{-1})	(–)	(–)	(cm^3 s^{-1})	
$NCCN^+ + e^- \rightarrow CN + CN$	1.00E-07	−0.5	0	5.48E-07	c
$HCNH^+ + e^- \rightarrow CH + NH$	1.50E-07	−0.5	0	8.22E-07	a
$NCHCN^+ + e^- \rightarrow HCN + CN$	1.00E-07	−0.5	0	5.48E-07	c
$NCHCN^+ + e^- \rightarrow NCCN + H$	1.70E-07	−0.5	0	9.70E-07	c
$HNCCN^+ + e^- \rightarrow HNC + CN$	1.00E-07	−0.5	0	5.48E-07	c
$HNCCN^+ + e^- \rightarrow NCCN + H$	1.70E-07	−0.5	0	9.70E-07	c
$HNCHCN^+ + e^- \rightarrow HNC + HCN$	1.50E-07	−0.5	0	8.22E-07	a
$HNCHCN^+ + e^- \rightarrow HCNH + CN$	1.50E-07	−0.5	0	8.22E-07	a
$HNCHCNH^+ + e^- \rightarrow E\text{-}HNCHCN + H$	1.50E-07	−0.5	0	8.22E-07	a
$HNCHCNH^+ + e^- \rightarrow HCNH + HCN$	1.50E-07	−0.5	0	8.22E-07	a
$HNCHCNH^+ + e^- \rightarrow HCNH + HNC$	1.50E-07	−0.5	0	8.22E-07	a

[a]Estimation according to analogous reaction rate coefficients in the OSU and KInetic Database for Astrochemistry (KIDA) network (Hasegawa et al. 1992; Garrod et al. 2007; Hassel et al. 2008; Quan et al. 2010; Wakelam et al. 2015).
[b]Rate coefficients for unmeasured reactions between ions and neutral species with a dipole moment are computed using the Su–Chesnavich capture approach. This approach is discussed in Woon & Herbst (2009) and Wakelam et al. (2010, 2012).
[c]Vastel et al. (2019); [d]Raksit et al. (1984); [e]Anicich (2003); [f]This work, based on potential and barrier calculations; [g]Vazart et al. (2015a); [h] Petrie et al. (2003).

to time by setting up and solving a series of ordinary differential equations (ODEs). The code was presented in detail by Reboussin et al. (2014) and Ruaud et al. (2016).

For this study, in addition to the cyanomethanimine chemistry and related reactions, our network also includes updates of the chemistry of HNCO and its metastable isomers (Quan et al. 2010), as well as the CH_3CHNH chemistry (Quan et al. 2016). We have added more than 400 reactions concerning the formation and destruction of the cyanomethanimine isomers and related species. A scheme of reactions relating to E-cyanomethanimine is shown in Fig. 1. As in Tables 2 and 3, the E-isomer is shown as an example. We use the standard oxygen-rich low-metal elemental abundances and initial abundances (Graedel, Langer & Frerking 1982; Quan & Herbst 2007) as listed in Table 4. All abundances are given with respect to the total hydrogen density. Desorption processes include thermal desorption, cosmic ray desorption, photodesorption via externally produced photons and via photons produced internally by cosmic rays (Öberg et al. 2007), and reactive desorption using the Rice–Ramsperature–Kessel (RRK) theoretical approach (Garrod et al. 2007).

3.2 Physical condition for models

In the two sources where cyanomethanimine isomers were detected, the physical conditions are rather complicated. Sgr B2(N) has a very complex cold-halo structure (Martín-Pintado et al. 1990; Hollis et al. 2004). It hosts several compact and ultracompact H II regions and five

Table 3. Summary of the rate coefficients of surface reactions involving E-cyanomethanimine.

Reaction Cosmic ray-induced photodissociation	α (–)	β (–)	γ (–)	k (10 K) (s^{-1})	Ref.
JE-HNCHCN → JHNC + JHCN	1.50E + 03	0	0	1.95E-14	a
JE-HNCHCN → JHCNH + JCN	1.50E + 03	0	0	1.95E-14	a
JE-HNCHCN → JNCHCN + JH	1.50E + 03	0	0	1.95E-14	a
JE-HNCHCN → JHNCCN + JH	1.50E + 03	0	0	1.95E-14	a
JHNCCN → JHNC + JCN	1.50E + 03	0	0	1.95E-14	a
JHNCCN → JNCCN + JH	1.50E + 03	0	0	1.95E-14	a
JNCHCN → JHCN + JCN	1.50E + 03	0	0	1.95E-14	a
JNCHCN → JNCCN + JH	1.50E + 03	0	0	1.95E-14	a
JNCCN → JCN + JCN	1.50E + 03	0	0	1.95E-14	a
JHCNH → JCH + JNH	1.50E + 03	0	0	1.95E-14	a
JHCNH → JHCN + JH	1.50E + 03	0	0	1.95E-14	a
JHCNH → JHNC + JH	1.50E + 03	0	0	1.95E-14	a
Photodissociation	(s^{-1})	(–)	(–)	(s^{-1})	
JE-HNCHCN → JHNC + JHCN	1.00E-09	0	1.9	5.60E-18	a
JE-HNCHCN → JHCNH + JCN	1.00E-09	0	1.9	5.60E-18	a
JE-HNCHCN → JNCHCN + JH	1.00E-09	0	1.9	5.60E-18	a
JE-HNCHCN → JHNCCN + JH	1.00E-09	0	1.9	5.60E-18	a
JHNCCN → JHNC + JCN	1.00E-09	0	1.9	5.60E-18	a
JHNCCN → JNCCN + JH	1.00E-09	0	1.9	5.60E-18	a
JNCHCN → JHCN + JCN	1.00E-09	0	1.9	5.60E-18	a
JNCHCN → JNCCN + JH	1.00E-09	0	1.9	5.60E-18	a
JNCCN → JCN + JCN	1.00E-09	0	1.9	5.60E-18	a
JHCNH → JCH + JNH	1.00E-09	0	1.9	5.60E-18	a
JHCNH → JHCN + JH	1.00E-09	0	1.9	5.60E-18	a
JHCNH → JHNC + JH	1.00E-09	0	1.9	5.60E-18	a
Surface reactions	E_a (K)			(cm^3 s^{-1})	
JCN + JCH_2NH → JE-HNCHCN + JH	9.05E-02			1.25E-22	a
JCN + JHCNH → JE-HNCHCN	0			1.97E-22	a
JNH + JH_2CCN → JE-HNCHCN + JH	0			4.04E-39	a
JNH + JHCCN → JE-HNCHCN	0			6.12E-39	a
Thermal desorption	E_D (K)	ν_i (s^{-1})		(cm^3 s^{-1})	
JE-HNCHCN → E-HNCHCN	4903	1.51E + 12		0.00	a, b
JHNCCN → HNCCN	4453	1.46E + 12		0.00	a, b
JNCHCN → NCHCN	4453	1.46E + 12		0.00	a, b
JNCCN → NCCN	3200	1.25E + 12		0.00	a, b
Cosmic ray desorption	E_D (K)	ν_i (s^{-1})		(cm^3 s^{-1})	
JE-HNCHCN → E-HNCHCN	4903	1.51E + 12		1.73E-37	a, b
JHNCCN → HNCCN	4453	1.46E + 12		1.03E-34	a, b
JNCHCN → NCHCN	4453	1.46E + 12		1.03E-34	a, b
JNCCN → NCCN	3200	1.25E + 12		5.24E-27	a, b
Photodesorption by external UV	$I_{ISRF-FU}$ (photons cm^{-2} s^{-1})		γ	(molecules cm^{-2} s^{-1})	
JE-HNCHCN → E-HNCHCN	1.00E + 08		2	1.37E-20	c
JHNCCN → HNCCN	1.00E + 08		2	1.37E-20	c
JNCHCN → NCHCN	1.00E + 08		2	1.37E-20	c
JNCCN → NCCN	1.00E + 08		2	1.37E-20	c
Photodesorption by CR generated UV	I_{CR-FU} (photons cm^{-2} s^{-1})			(molecules cm^{-2} s^{-1})	
JE-HNCHCN → E-HNCHCN	1.00E + 04			6.67E-16	c
JHNCCN → HNCCN	1.00E + 04			6.67E-16	c
JNCHCN → NCHCN	1.00E + 04			6.67E-16	c
JNCCN → NCCN	1.00E + 04			6.67E-16	c
E-HNCHCN → JE-HNCHCN	3.14E-10	6.26E + 03		5.19E-14	a
HNCCN → JHNCCN	3.14E-10	6.32E + 03		5.24E-14	a
NCHCN → JNCHCN	3.14E-10	6.32E + 03		5.24E-14	a
NCCN → JNCCN	3.14E-10	6.38E + 03		5.29E-14	a

[a]Estimation according to analogous reaction rate coefficients in the OSU and KIDA network (Hasegawa et al. 1992; Hasegawa & Herbst 1993; Garrod et al. 2007; Hassel et al. 2008; Quan et al. 2010; Wakelam et al. 2015).
[b]E_D(E-HNCHCN) = E_D(CN) + E_D(HCNH); E_D(HNCCN) = E_D(NCHCN) = E_D(E-HNCHCN) − E_D(H); E_D(NCCN) = E_D(N) + E_D(CCN).

hot cores – Sgr B2(N1–N5) – in Sgr B2(N) (Belloche et al. 2016; Bonfand et al. 2017). The quiescent giant molecular clouds G+0.693 are located towards the north-east of the Sgr B2 star formation region.

We utilized several different physical models in the study. The major physical parameters of the constant and warm-up models are summarized in Table 5. In the first set, the physical parameters remain constant with a hydrogen density of $n_H = n(H) + 2n(H_2)$

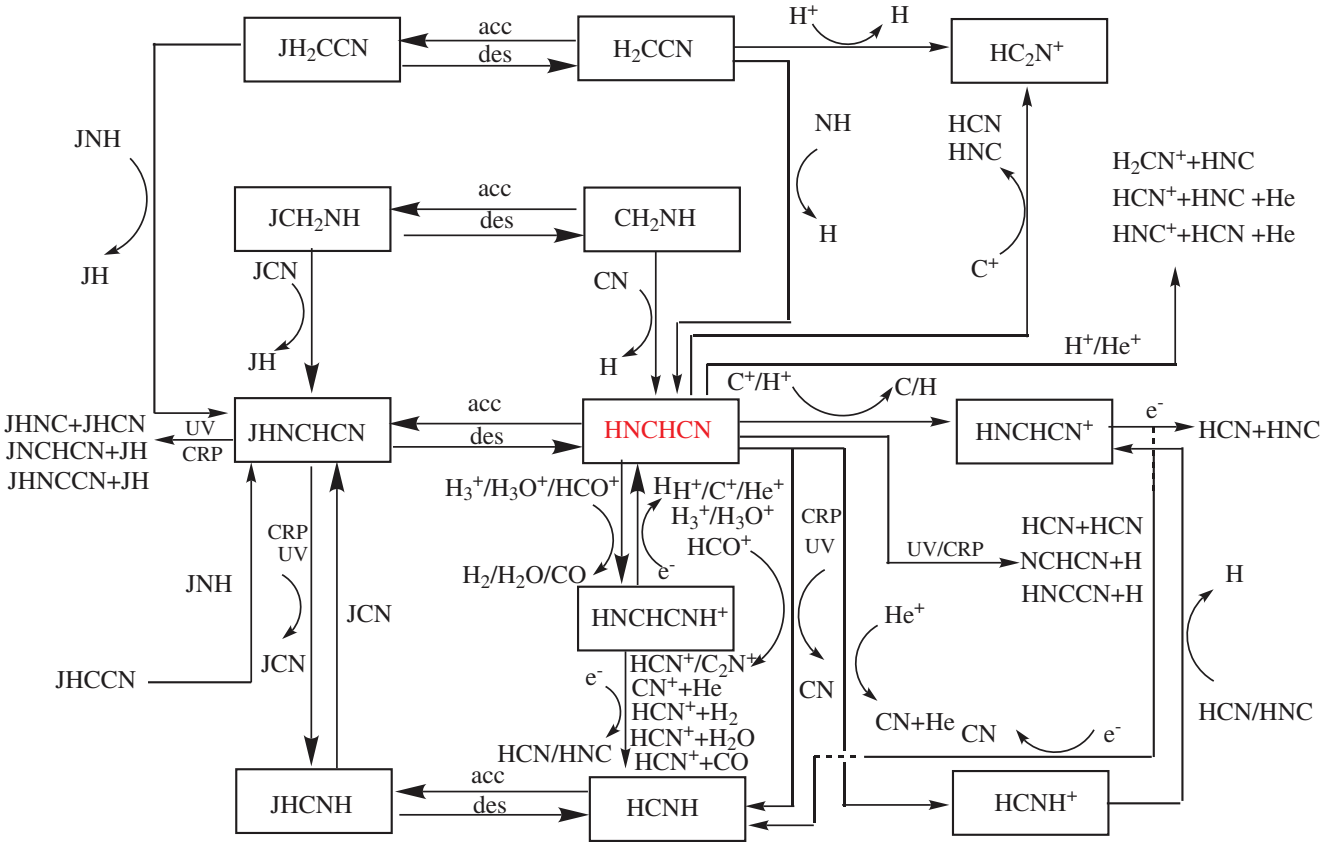

Figure 1. Gas-phase and surface reactions of cyanomethanimine and related species. The E-isomer is shown as an example, the Z-cyanomethanimine and N-cyanomethanimine isomers have similar reactions.

Table 4. Initial fractional abundances with respect to total hydrogen density.

Species	Abundance
He	6.00×10^{-2}
N	2.14×10^{-5}
O	1.76×10^{-4}
H_2	5.00×10^{-1}
C^+	7.30×10^{-5}
S^+	8.00×10^{-8}
Si^+	8.00×10^{-9}
Fe^+	3.00×10^{-9}
Na^+	2.00×10^{-9}
Mg^+	7.00×10^{-9}
P^+	3.00×10^{-9}
Cl^+	4.00×10^{-9}
F^+	6.69×10^{-9}

$= 2 \times 10^4$ cm^{-3}, gas and grain temperatures of 10, 30, and 50 K, a visual extinction A_V of 10 mag, a cosmic ray ionization rate ζ of 1.3×10^{-17} s^{-1}, and a single grain radius of 0.1 μm (Model 1 in Table 5; Hasegawa et al. 1992).

In the second set, we performed calculations with warm-up models with hydrogen densities with an assortment of values. After an initial cold phase of 1×10^5 yr where $T = 10$ K, the gas and dust temperatures increase to maximum temperatures T_{max} of 30 and 50 K within a time frame of 2×10^5 yr. After reaching the maximum value, the temperature remains unchanged (Model 2 in Table 5; Garrod & Herbst 2006). For maximum temperatures T_{max} of 100, 150, and 200 K, we adopted two types of constant hydrogen density of $n_H = 2 \times 10^5$ and 2×10^6 cm^{-3} (Models 3 and 4 in Table 5).

The sources Sgr B2(N) and the molecular cloud G+0.693 are both near the GC, which is known to contain external heating sources such as cosmic rays, shocks, a strong UV field, and X-ray sources. Most of the heating in the clumps is likely internal, but in some places, external heating may play a significant role, even for small clumps (Ott et al. 2014). Clumps denote ∼1 pc molecular cloud structures (Motte et al. 2018). To partially take account of these conditions, we also use a higher cosmic ray ionization rate of 1.3×10^{-16} s^{-1} (Model 4 in Table 5). The value agrees with the view that the cosmic ray ionization rate in Sgr B2 is an order of magnitude larger than in the Galactic disc (Van der Tak et al. 2006; Crocker et al. 2007; Bonfand et al. 2019).

3.3 C-type shock model

The Sgr B2(N) molecular cloud contains a complex of H II regions near the Galactic Centre where intense star formation is taking place. It is known as one of the most luminous massive star-forming regions in our Galaxy, with a total bolometric luminosity of $\sim 10^7$ L$_\odot$ in a diameter of ∼40 pc (Lis & Goldsmith 1989, 1990, 1991). Since the dust is too cold (10–20 K) for the desorption of the ice mantles, it has been suggested that the sputtering of the grains and grain mantles produced by widespread shocks with moderated velocities is responsible for the rich chemistry and the high temperatures observed in the Central Molecular Zone (CMZ; Hüttemeister et al.

Table 5. Physical parameters of models.

Parameter	Model 1	Model 2 (warm-up 1)	Model 3-1/2 (warm-up 2)	Model 4-1/2 (warm-up 3)
n_H (cm^{-3})	2×10^4	2×10^4	$2 \times 10^5(10^6)$	$2 \times 10^5(10^6)$
T (K)	10/30/50	30/50	100/150/200	100/150/200
ζ (s^{-1})	1.3×10^{-17}	1.3×10^{-17}	1.3×10^{-17}	1.3×10^{-16}
A_V (mag)	10	10	10	10
d/g	0.01	0.01	0.01	0.01
a_{RRK}	0.01	0.01	0.01	0.01
UV factor (Habing)	1	1	1	1

Note. d/g, dust-to-gas ratio by mass.

Table 6. Physical parameters of C-type shock model.

Parameter	Value
Initial density n_H (cm^{-3})	2×10^4
Pre-shock temperature (K)	10
Radiation field (Habing) UV factor	1
Cosmic ray ionization rate ζ (s^{-1})	1.3×10^{-17}
Visual extinction A_V (mag)	10
Magnetic field strength parameter b	1.0
Shock speed u_s (km s^{-1})	10

1998; Martín-Pintado et al. 1999, 2001; Chengalur & Kanekar 2003). Regarding the quiescent giant molecular clouds G+0.693, it has been proposed that this source is located between two streams of molecular gas that seem to be merging (Hasegawa et al. 1994; Henshaw et al. 2016). This process may yield a cloud–cloud collision that will drive large-scale, low-velocity shocks in the region, and which ultimately sputters icy mantles of grains efficiently. For the shock model, we use the NAUTILUS code combined with the planar magnetohydrodynamic (MHD) shock code MHD_VODE to simulate the chemical evolution of cyanomethanimine isomers under shock conditions.

The planar MHD shock code MHD_VODE (Flower & Pineau des Forêts 2015) has been developed in order to simulate both continuous (C-type) and jump (J-type) shock waves in the interstellar medium. In this study, we only use the C-type shock wave model. We start the calculations by simulating the gas–grain chemistry that occurs in the cold molecular clouds for 3×10^5 yr. The pre-shock density was set to the hydrogen density of 2×10^4 cm^{-3}, with an extinction of 10 mag, and a cosmic ray ionization rate ζ of 1.3×10^{-17} s^{-1}.

Shock waves can affect the cold regions towards Sgr B2(N) or some boundaries of star formation regions in our shock models. We use parameters obtained from the physical structure of the shock, which is computed by the shock code. The parameters include time, visual extinction, temperature, and hydrogen density. We have considered weak shocks with a speed of 10 km s^{-1}, and an initial temperature of 10 K. The interaction between the gas and grains with the magnetic field is crucial for the development of C-type shock waves. We used a magnetic field strength parameter $b = 1.0$, leading to a transverse field strength $B_0 = b \times (n_H)^{1/2}$ μG (Troland & Heiles 1986). The major physical parameters of the C-type shock wave model are summarized in Table 6.

In Fig. 2, the left-hand panel shows the dependence of density and temperature on the time of the stationary gas, while the right-hand panel shows the corresponding variation of density and visual extinction with time. The time-scale of a shock depends on its velocity and initial conditions of the cloud. In the left-hand panel, the time of the flow through a C-type shock wave can be seen, from the pre-shock to the post-shock, and to the equilibrium gas, within a time-scale on the order of 10^5 yr in our models. In Fig. 2, $t = 0$ represents the onset of the shock. After the shock, the gas temperature can reach more than several hundred Kelvin. When the gas cools, the density rises as a result of pressure equilibrium and remains high after 1×10^4 yr. As shown in the right-hand panel, while the density increases, the extinction A_V also increases as a function of time. As the density reaches a steady state at approximately 10^4 yr, the visual extinction continues to increase.

4 RESULTS

Sgr B2(N) has a complex structure, including hot cores and a cold envelope. Because the H_2 column density of the observed region is unclear, to evaluate the fractional abundances of E-cyanomethanimine toward Sgr B2(N), we use hydrogen column densities of 4.0×10^{23} cm^{-2} for the envelope and 1.54×10^{25} cm^{-2} for the hot cores (Quan et al. 2016; Bonfand et al. 2017). For the quiescent giant molecular clouds G+0.693, we adopt the hydrogen column densities of 1.35×10^{23} cm^{-2} derived by Martín et al. (2008) from $C^{18}O$.

The models that are relevant to cold envelopes are the isothermal ones and the warm-up models to lower maximum temperatures.

In Figs 3 and 4 and Figs 6–10, we plot calculated fractional abundances of cyanomethanimine isomers with respect to time for isothermal and assorted warm-up models and compare them with observations (Zaleski et al. 2013). In Figs 3 and 4 and Figs 6–9, we use the purple rectangles to represent the observed abundance toward Sgr B2(N). In Fig. 10, we use the same legend (lower rectangles) for Sgr B2(N), and the grey rectangles (upper) to represent the observed abundances toward G+0.693. In all cases, we include a factor of ±3 uncertainty for the observed values. The special case of G+0.693, a galactic quiescent cloud, with an isomeric ratio of Z to E of 6:1, is treated separately below. We use the term 'sufficient' regarding calculated abundances if they agree with observations to within an order of magnitude.

4.1 Results for isothermal and warm-up models

Fig. 3 shows that the isothermal model (Model 1) produces very low gaseous abundances of all three isomers of cyanomethanimine at 10, 30, and 50 K. Comparison with the observation of the E-isomer in Sgr B2(N) shows that the calculated abundance is at least one order of magnitude lower than the observed values in the investigated time range. In the gas, the main formation route of the cyanomethanimine isomers at these temperatures occurs via reactions (1)–(3) ($CN + CH_2NH$). Because the CN abundance is larger than the NH abundance, reactions (4) and (5) ($NH + H_2CCN$) produce less E- and Z-cyanomethanimine than reactions (1) and (2) do. At 10 K, the surface cyanomethanimine isomers mainly come from their gaseous counterparts by accretion on to the grain surface.

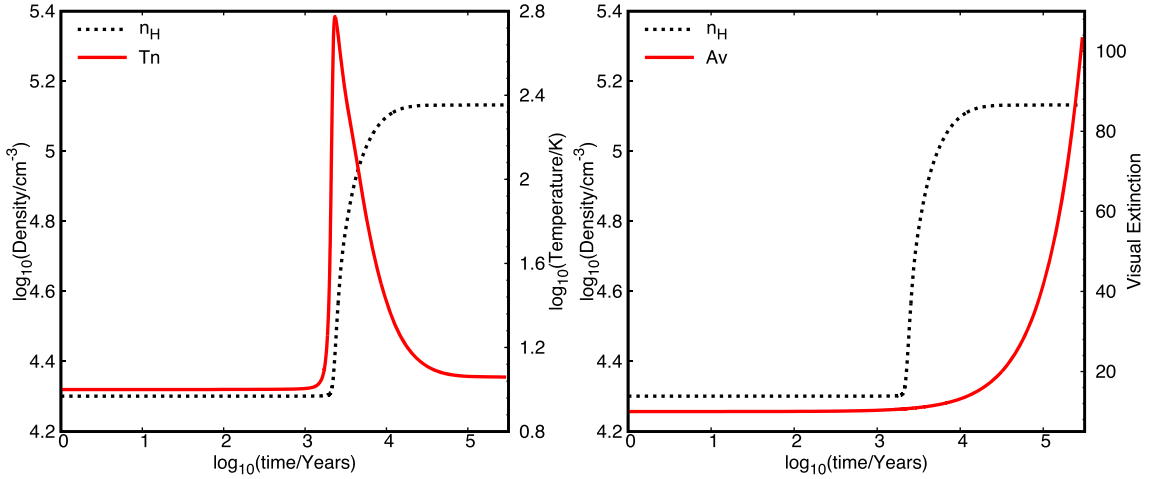

Figure 2. The density, temperature, and A_V profiles as functions of time for a shock wave of speed $u_s = 10$ km s^{-1} propagating into gas of density 2×10^4 cm^{-3} in which the transverse magnetic field strength $B_0 = 141$ μG.

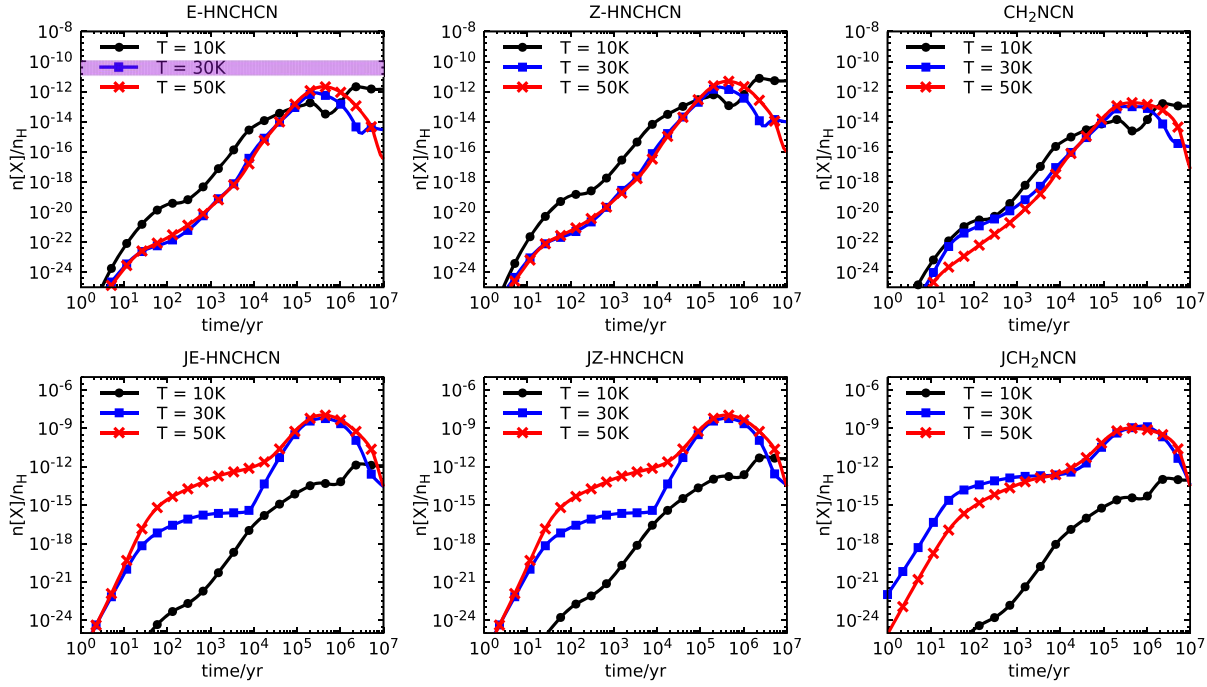

Figure 3. The calculated abundances of the Z-, E-, and N-isomers of cyanomethanimine in the gas phase and on grain mantles are plotted versus time for the isothermal model (Model 1) at temperatures of 10, 30, and 50 K. In this figure and in Figs 4 and 6–9, the purple rectangles represent the observed abundance of the E-isomer in Sgr B2(N).

So we can deduce that the gaseous cyanomethanimine isomers are mainly produced by gas-phase reactions at this temperature. At 30 and 50 K, the surface isomers are produced mainly by the reactions JCN + $JCH_2NH \rightarrow$ JHNCHCN + JH, JCH_2NCN + JH and JCN + JHCNH → JHNCHCN, JCN + $JH_2CN \rightarrow$ JCH_2NCN on the grain surface and weakly desorbed into the gas. The major destruction reactions are by cosmic ray-induced photodissociation.

As is clear from Fig. 4, the warm-up models (Model 2) with low maximum temperatures of 30 and 50 K are also ineffective in producing sufficient abundances of gaseous cyanomethanimine isomers. In the gas phase, cyanomethanimine molecules are mainly produced by the reactions CN + $CH_2NH \rightarrow$ HNCHCN, CH_2NCN + H and also by reactions NH + $H_2CCN \rightarrow$ HNCHCN + H, CH_2NCN + H. The temperature is still not high enough to produce sufficient complex molecules such as the cyanomethanimine isomers in the gas phase. But the cyanomethanimine isomers are efficiently produced on the grain surface after 2×10^5 yr. The main formation route is the reaction JCN + JCH_2NH, which produces all three isomers at an increased rate at temperatures higher than 10 K. The fractional abundances of the granular cyanomethanimine isomers each reach values of 10^{-8} when the higher temperatures are reached.

Fig. 5 shows the effects of thermal desorption for gaseous E-cyanomethanimine using Model 3 except that a larger number of maximum temperatures are used. For each run, the fractional

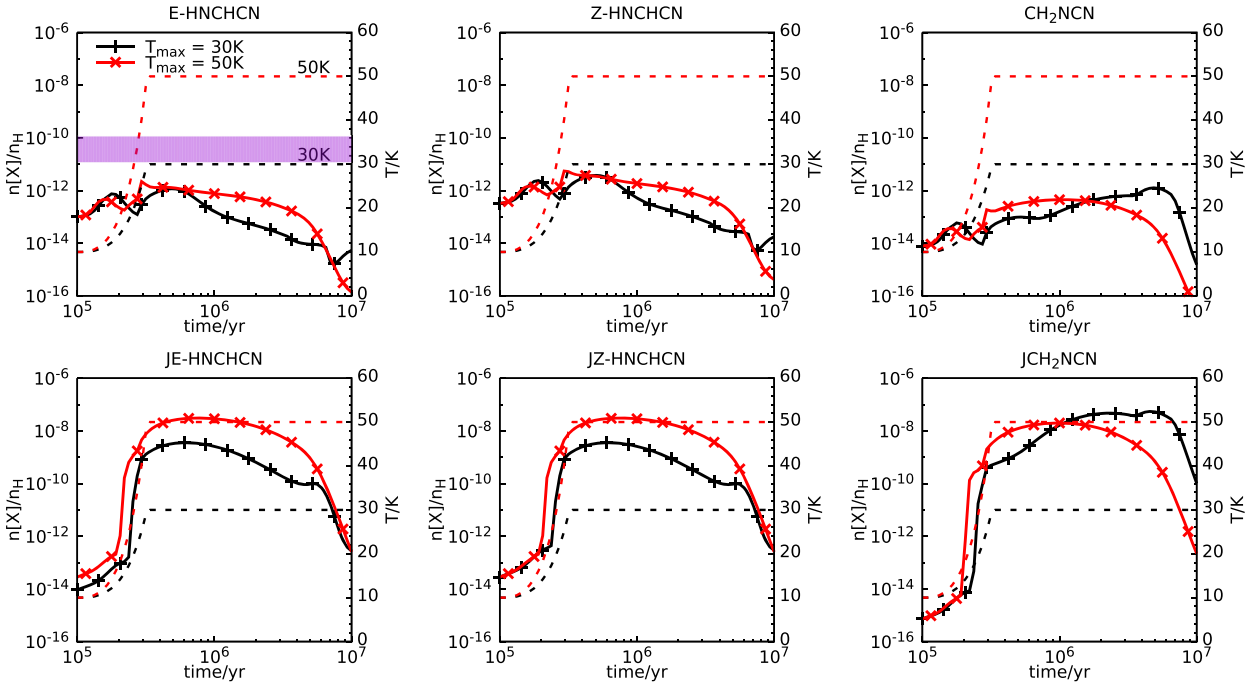

Figure 4. The calculated abundances of the Z-, E-, and N-isomers of cyanomethanimine in the gas phase and on grain mantles are plotted versus time for warm-up model 1 (Model 2) with $n_{\rm H} = 2 \times 10^4$ cm^{-3}, $\zeta = 1.3 \times 10^{-17}$ s^{-1}, and $T_{\rm max} = 30$ and 50 K. The time ranges from the beginning of the warm-up through the post-warm-up period as indicated by the temperature.

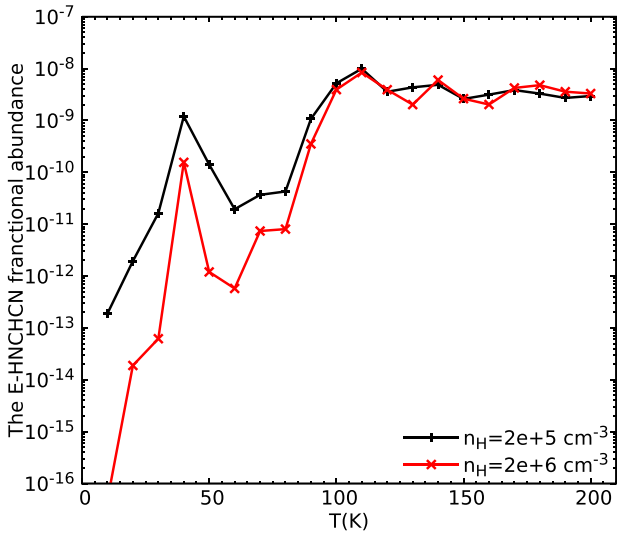

Figure 5. The fractional abundances of the gaseous E-isomers are plotted against maximum asymptotic temperature at a time of 3×10^5 yr for warm-up model with $n_{\rm H} = 2 \times 10^5$ and 2×10^6 cm^{-3}, $\zeta = 1.3 \times 10^{-17}$ s^{-1}.

abundance of the gaseous E-isomer is plotted against maximum asymptotic temperature at a time of 3×10^5 yr at which time desorption is the dominant synthetic mechanism. It can be seen that by a maximum temperature of 100 K, a nearly constant fractional abundance between 10^{-8} and 10^{-9} is reached. The gaseous Z- and N-isomers show a similar effect due to thermal desorption, but here we only show the E-isomer as an example. The calculated E-isomer abundance undergoes a sharp increase, also due to thermal desorption, at maximum temperatures reaching around 90 K in the gas phase. When the maximum temperatures lie in the range 90–100 K, the calculated E-isomer abundances increase slowly as gas-phase destructive reactions are effective. Concerning thermal desorption, there are small discrepancies between the two different hydrogen densities plotted.

Figs 6 and 7 show that the warm-up models (Models 3-1 and 3-2) can produce sufficient abundances of the cyanomethanimine isomers during the warm up to maximum temperatures of 100, 150, and 200 K, but when the temperature reaches its maximum values, the calculated abundances are far too large, so that optimum temperatures for agreement are in the range 20–80 K for $n_{\rm H} = 2 \times 10^5$ cm^{-3} (Fig. 6), and the range 40–80 K for $n_{\rm H} = 2 \times 10^6$ cm^{-3} (Fig. 7). Before the warm-up begins, the gaseous isomers are once again mainly produced by the reaction between CN and CH_2NH in the gas phase. When the temperature begins to increase after 1×10^5 yr, NH and H_2CCN start to contribute to the isomeric abundances as they begin to reach their peaks in the gas phase. At a time of 2×10^5 yr, the abundances reach their maxima as results of thermal desorption, which becomes efficient at increasing temperature. Afterwards, the cyanomethanimine abundances decline due to effective gas-phase destruction reactions, especially those by positive ions such as H^+, H_3^+, C^+, and H_3O^+. On the grain surface, the cyanomethanimine isomers show strong increases in abundance with increasing temperatures because the thermal energy becomes sufficient in overcoming the diffusion barriers of the surface formation reactions. But eventually, the surface isomers desorb into the gas phase by thermal desorption. This is essentially the mechanism introduced by Garrod & Herbst (2006) and Garrod et al. (2008).

Figs 8 and 9 show that all three cyanomethanimine isomers can be sufficiently produced at maximum temperatures of 100, 150, and 200 K with a higher cosmic ray ionization rate (Models 4-1 and 4-2). But, due to the higher rate, the abundances of the gas-phase cyanomethanimine isomers during warm-up are lower than those in Models 3-1 and 3-2 by at least one order of magnitude. This effect

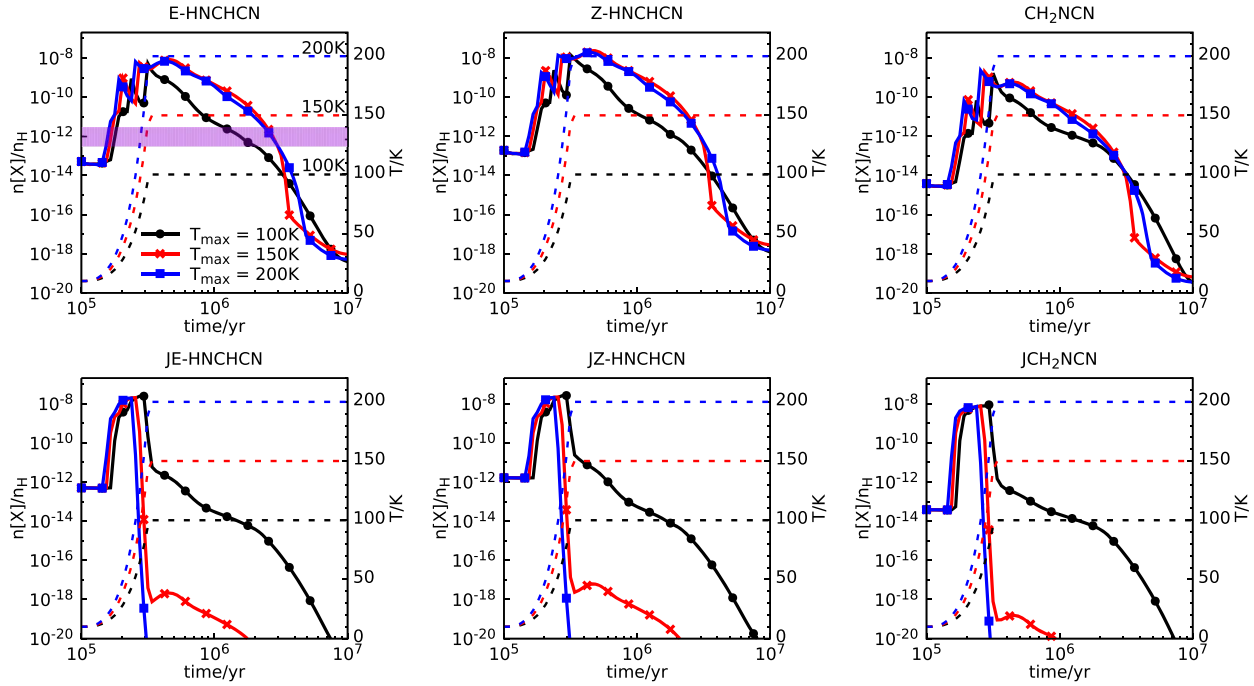

Figure 6. The calculated abundances of the Z-, E-, and N-isomers of cyanomethanimine in the gas phase and on grain mantles are plotted versus time for warm-up model 2 (Model 3-1) with $n_{\rm H} = 2 \times 10^5$ cm^{-3}, $\zeta = 1.3 \times 10^{-17}$ s^{-1}, and $T_{\rm max} = 100$, 150, and 200 K.

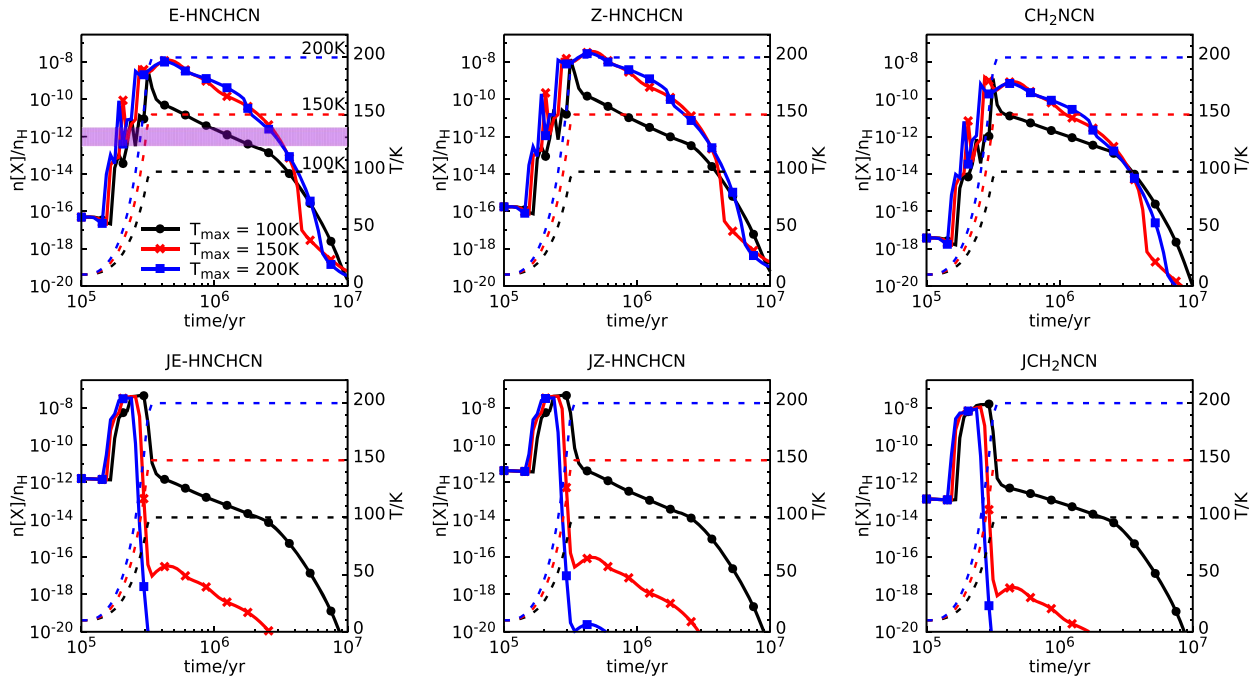

Figure 7. The calculated abundances of the Z-, E-, and N-isomers of cyanomethanimine in the gas phase and on grain mantles are plotted versus time for warm-up model 2 (Model 3-2) with $n_{\rm H} = 2 \times 10^6$ cm^{-3}, $\zeta = 1.3 \times 10^{-17}$ s^{-1}, and $T_{\rm max} = 100$, 150, and 200 K.

leads to lower calculated values at peak abundance and a reasonable agreement with observation within the time period 1–5 $\times$ 10^5 yr.

According to observations of Melosso et al. (2018) with the IRAM 30-m dish, the abundance of Z- and E-cyanomethanimine is $\leq 4 \times 10^{-10}$ for starless cores and hot-corinos and $\leq 10^{-11}$ for Sgr B2(N), the latter in agreement with the earlier positive identification of $\approx 10^{-12}$ for the E-isomer. The low abundance for Sgr B2(N) can be best fit by our Models 4-1 and 4-2, which show calculated values around the value of $\approx 10^{-12}$ for significant periods of time (1–5 $\times$ 10^5 yr) near the peak temperature. Another possibility is a large halo with a lower than average column density of hydrogen, which would raise the fractional abundance of cyanomethanimine.

4.2 Results of shock models

In cold conditions, the ejection of molecules from the grain surface into the gas phase by desorption is slow, but this process can be quickened by shocks with moderate velocities. The shock heats

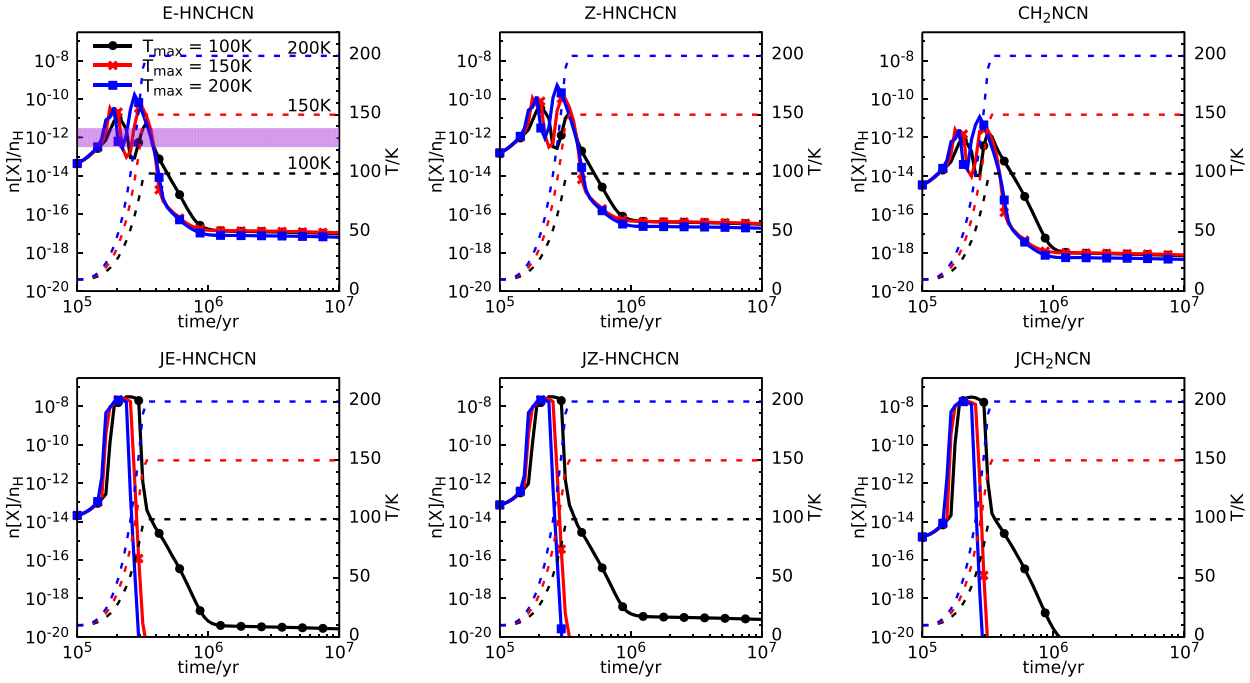

Figure 8. The calculated abundances of the Z-, E-, and N-isomers of cyanomethanimine in the gas phase and on grain mantles are plotted versus time for warm-up model 3 (Model 4-1) with $n_{\rm H} = 2 \times 10^5$ cm^{-3}, $\zeta = 1.3 \times 10^{-16}$ s^{-1}, and $T_{\rm max} = 100$, 150, and 200 K.

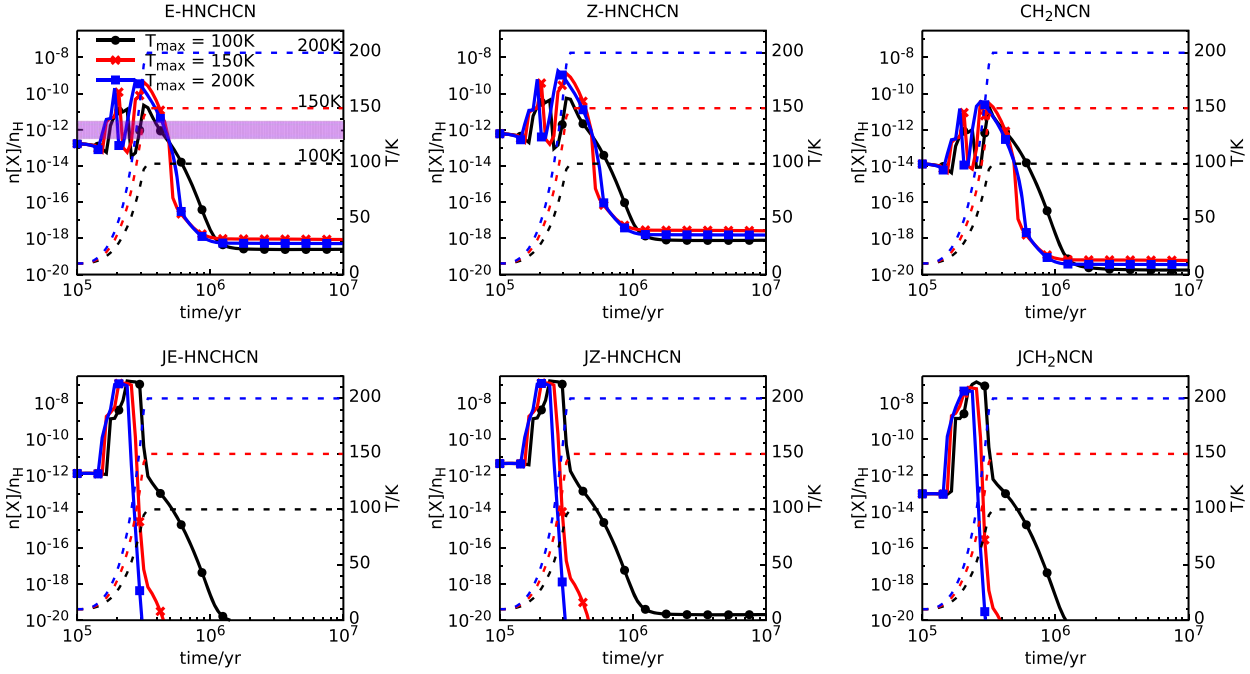

Figure 9. The calculated abundances of the Z-, E-, and N-isomers of cyanomethanimine in the gas phase and on grain mantles are plotted versus time for warm-up model 3 (Model 4-2) with $n_{\rm H} = 2 \times 10^6$ cm^{-3}, $\zeta = 1.3 \times 10^{-16}$ s^{-1}, and $T_{\rm max} = 100$, 150, and 200 K.

the grain and produces the sputtering of molecules from the grain mantles. For shock velocities of ∼10 km s^{-1}, the gas temperature can reach hundreds of Kelvin. After the shock passage, the gas cools on time-scales of ∼10^5 yr for final densities of 10^5 cm^{-3}. Fig. 10 shows that the C-type shock model, with physical parameters shown in Table 6, can produce reasonable abundances of cyanomethanimine isomers compared with observed values toward Sgr B2(N) and G+0.693 at times of 10^4–10^5 yr (Zaleski et al. 2013; Rivilla et al. 2019), with different initial cloud core conditions. The simulated results coincide with the upper limit of observed abundances ∼10^{-9} at all the investigated shock sources by Melosso et al. (2018).

Before ∼2×10^3 yr, the gaseous cyanomethanimine isomers are mainly formed by the reaction of CN + CH_2NH in the gas phase, while between 2×10^3 and 3×10^3 yr, as the temperature increases rapidly in a short amount of time, thermal desorption contributes to the abundance of gas-phase cyanomethanimine. Meanwhile the

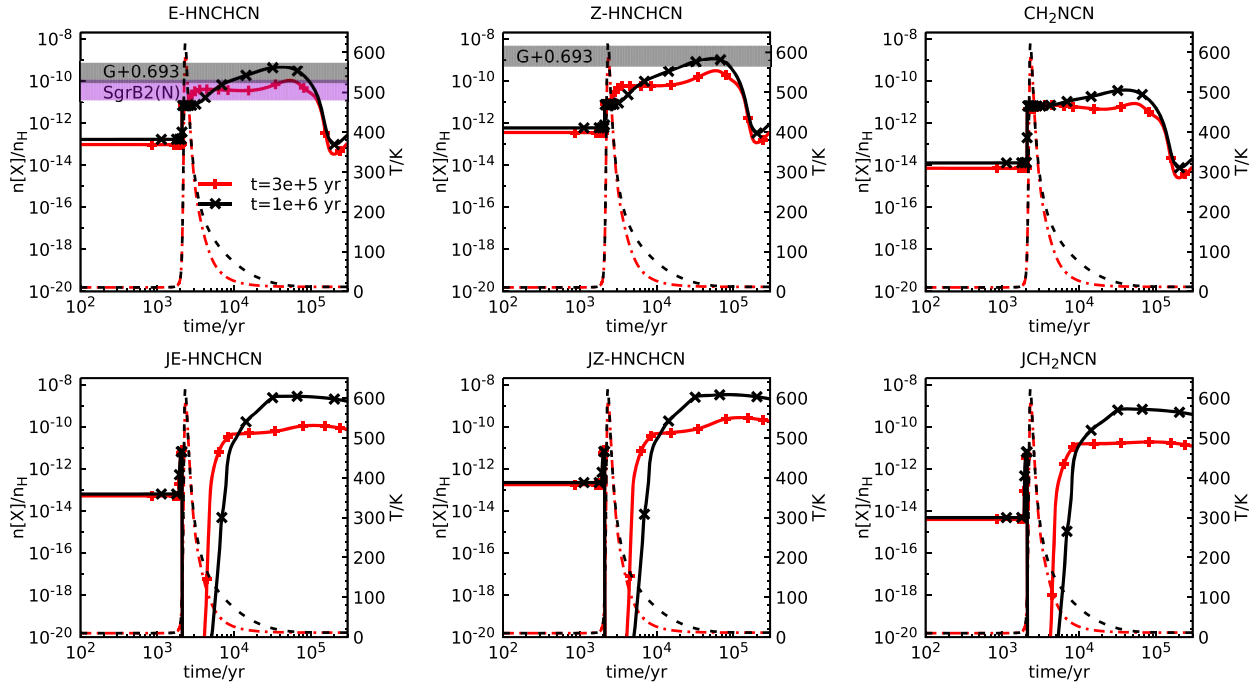

Figure 10. Abundances of cyanomethanimine molecules as a function of time for our C-type shock model with initial temperature of 10 K, shock wave of speed $u_s = 10$ km s^{-1}, and $\zeta = 1.3 \times 10^{-17}$ s^{-1} propagating into gas of density $n_H = 2 \times 10^4$ cm^{-3}. The transverse magnetic field strength $B_0 = 141$ μG. The red lines with pluses refer to the time before the shock onset, during which time the model runs for 3×10^5 yr using standard cold core conditions, while the black lines with crosses refer to a pre-shock onset that runs for 1×10^6 yr using standard cold core conditions. The purple area (lower) refers to the observed abundance ± a factor of 3 uncertainty in Sgr B2(N), while the grey area (upper) refers to the observed abundance ± a factor of 3 uncertainty in the molecular cloud G+0.693. The dashed lines correspond to temperature profiles.

major formation reaction becomes NH + H_2CCN. As temperature subsequently decreases, the gas-phase reaction CN + CH_2NH once again plays an important role in producing the cyanomethanimine isomers. After ∼10^4 yr, the temperature almost returns to 10 K, and the cyanomethanimine abundance declines.

Before ∼2×10^3 yr, cyanomethanimine isomers on the grain surface mainly are produced by depletion from the gas phase, as the large molecules possess diffusion barriers high enough to hinder surface reactions. At ∼2×10^3 yr, as the temperature increases sharply, the abundance of surface cyanomethanimine increases quickly, as JCN + JCH_2NH can effectively produce them. After that time, thermal desorption largely reduces the abundance of surface species. As the temperature returns to lower values, thermal desorption becomes weak again, and the reaction between JCN and JCH_2NH recovers its importance. By a time of 10^4 yr, the production of surface cyanomethanimine mainly comes from the gaseous species accreting on grain surface, similar to the case under pre-shock conditions. One of the two chemical pathways proposed by Rivilla et al. (2019) to form cyanomethanimines by grain sputtering in moderate-velocity shock waves is similar to the pathway in our shock models, in which surface reactions with moderate-velocity shock waves can lead to the formation of gaseous cyanomethanimine in molecular clouds.

Although not discussed in detail here, we also studied the case of a hot core that is influenced by a shock. The hot core model was run for 3×10^5 yr during which the abundances of the cyanomethanimine isomers reach their peak values of ∼10^{-8} (E-, Z-isomers) and 10^{-9} (N-isomer) in the gas phase before the onset of the shock. From Fig. 5, it can be seen that when the temperature reaches about 100 K, the abundance of the E-isomer increases slowly, and the Z- and N-isomers also have similar trends. So when shocks arrive, the abundances of the cyanomethanimine isomers are only slightly increased. We found that the calculated abundances of the cyanomethanimine isomers quickly decrease at times of 3×10^4 yr after the shock effect.

4.3 Shock tracers

Several research groups have suggested that the sulphur-bearing species SO, SO_2, and H_2S are enhanced in shocks and hence are potential tracers of shock activity (Friberg 1984; Blake et al. 1987; Stutzki et al. 1989; Pineau des Forets et al. 1993; Holdship et al. 2016). We have looked at the variation in abundance of some these sulphur-bearing species in our shock model. The fractional abundances of SO, SO_2, and H_2S are plotted against time in Fig. 11. Our calculations show that the fractional abundance of H_2S is enhanced by about two orders of magnitude at time 2×10^3 yr compared with the pre-shock conditions. The enhancement occurs in the following manner. H_2S is unlikely to be produced by low-temperature hydrogenation reactions of S + H_2 → H + HS, HS + H_2 → H + H_2S in gas phase because they have high activation energies (Pineau des Forets et al. 1993). Instead, H_2S is mainly produced by the surface reaction of JH + JHS → JH_2S under cold cloud conditions, with the result that a significant fraction of the sulphur is locked in the form of H_2S on the grains at low temperature. When a shock passes, the temperature increases, and H_2S is desorbed from the grain surface to the gas phase. Unlike H_2S, the fractional abundance of SO is only enhanced by less than one order of magnitude at 2×10^4 yr, as demonstrated in Fig. 11.

In our shock model, SO is mainly produced initially by the reaction of S + OH → SO + H. Because SO_2 is mainly formed by the reaction of OH + SO → SO_2 + H, it can be efficiently produced only when there is a high abundance of SO. SO_2 is enhanced by one order of

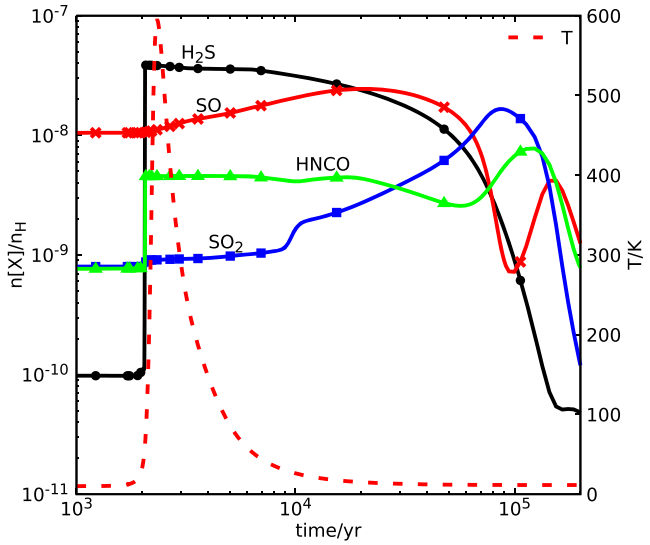

Figure 11. Simulated abundances of the SO, SO_2, H_2S, and HNCO molecules as a function of time for our C-type shock model with initial temperature of 10 K, shock wave of speed $u_s = 10$ km s^{-1} and $\zeta = 1.3 \times 10^{-17}$ s^{-1} propagating into a gas of density $n_H = 2 \times 10^4$ cm^{-3}. The transverse magnetic field strength $B_0 = 141$ μG. Before the onset of the shock, the model was initially run for 3×10^5 yr using standard cold core conditions. The dashed line represents the temperature profile.

magnitude at time 1×10^5 yr. We can conclude that sulphur-bearing species reach their peak values at different times. Therefore, SO, SO_2, and H_2S can be related to the evolution of a shock as they are all enhanced by the shock process. There are many observational results for sulphur-bearing species in the Sgr B2(N) region (Nummelin et al. 2000; Belloche et al. 2013; Neill et al. 2014). In comparison with the results from Belloche et al. (2013) for Sgr B2(N), we found that the simulated H_2S abundance lies within an order of magnitude of their observed value, but the simulated SO and SO_2 values are less than the observed values by one order of magnitude. Note however that we use a depleted abundance of elemental sulphur (8×10^{-8}) rather than the cosmic value (Wakelam & Herbst 2008) so that we could calculate higher abundances of sulphur-bearing species with a higher sulfur abundance. In Vidal et al. (2017), the authors studied in some detail the effect of using different elemental abundances of sulphur. While they used the initial elemental abundance of elemental sulphur as 8×10^{-8} for dark cloud conditions and computed the SO peak abundance to be 1×10^{-8} in the gas phase, our shock model result shows that the SO peak abundance is twice their value. For H_2S, the simulated peak abundance from Vidal et al. (2017) is only 10^{-10}, while the value can be increased by more than two orders of magnitude using our shock model even with the low sulphur abundance.

In hot cores, the temperature increase can also effectively cause sulfur-bearing species to desorb from the dust grains via the thermal process. Therefore we also compared the results from hot core models with those from shock models. We found that in both hot core and shock models, the abundances of the gas-phase sulfur species SO, SO_2, and H_2S all increase significantly and can reach a maximum value of 10^{-8}.

In addition, we studied HNCO in the shock model since the molecule is supposed to be one of the common observational shock tracers (Rodríguez-Fernández et al. 2010; Kelly et al. 2017). HNCO can be formed in the gas phase during the cold stages, followed by freezing out on to the icy mantles (López-Sepulcre et al. 2015), or can be formed mainly on dust grain mantles (Fedoseev et al. 2015). Our shock result shows that the HNCO is mainly produced by the H + OCN → HNCO reaction on grain surfaces at low temperature. When a shock passes, the temperature increases, and HNCO is desorbed from the grain surface to the gas phase. Therefore, granular HNCO is located on the outer monolayers of the dust mantle rather than closer to the core. This means that it is easily desorbed even in weakly shocked regions, hence HNCO may be a particular tracer of low-velocity shocks (Kelly et al. 2017). From Fig. 11, it can be seen that the abundance of HNCO is enhanced by one order of magnitude at a time of 1×10^5 yr compared with its pre-shock value. The computed abundance of HNCO is one order of magnitude lower than the observational peak results from Sgr B2(N) (Belloche et al. 2013). We conclude that HNCO also can be related to the evolution of a shock as it is enhanced by the shock process.

4.4 Isomeric abundance ratios

Figs 12 and 13 present the time evolution of the gas-phase Z-/E-cyanomethanimine abundance ratio for various models. In Fig. 12, we show the ratio from isothermal and warm-up models. It can be seen that the computed ratios lie mainly in the range of 2–5 from the results of isothermal and warm-up models. This range of values roughly agrees with the value obtained from the observed Z/E ratio of ∼6 in the source G+0.693 (Rivilla et al. 2019). The main reason for the abundance difference between the E- and Z-isomers is that they have the different rate coefficients for gas-phase cation–neutral destruction reactions. Because of the lower dipole moment of the Z-isomer, the rate coefficients of related reactions are smaller than those of for the E-isomer. The N-isomer has both a lower formation rate and higher destruction rate compared with the E- and Z-isomers. All these account for the different abundances of the cyanomethanimine isomers.

When the high cosmic ray ionization rate is used, the calculated ratio is lower, as shown in the right-hand panel. For warm-up models, the best agreement occurs when temperatures are increasing and the cosmic ray ionization rate is at its standard value.

Fig. 13 shows a similar comparison for shock models. The Z/E ratio is in the range of 1–5 and the peak occurs at $t \sim 1$–2×10^5 yr when the final evolutionary age of the shock is reached. The modelled ratio is also close to the observed value of Rivilla et al. (2019).

5 SUMMARY

In this study, we added over 400 chemical reactions involving cyanomethanimine isomers and their related species to the gas–grain version of NAUTILUS in order to study cyanomethanimine chemistry. We used a two-phase gas–grain model to simulate the physical conditions where cyanomethanimines have been observed and might be detected in the future. We established three sets of physical conditions, including cold/lukewarm isothermal models, warm-up models, and C-type shock models. The abundance range of cyanomethanimines is not very high compared with other simple COMs. Interferometric detection, however, using the Atacama Large Millimeter/submillimeter Array (ALMA), NOrthern Extended Millimeter Array (NOEMA), and the Very Large Array (VLA) with higher spatial resolution and sensitivity will make it more possible to detect these molecules in other interstellar sources.

Of all models applied, the warm-up models with standard and higher cosmic ray ionization rates both yield gaseous cyanomethanimine abundances in good agreement with observations at time-

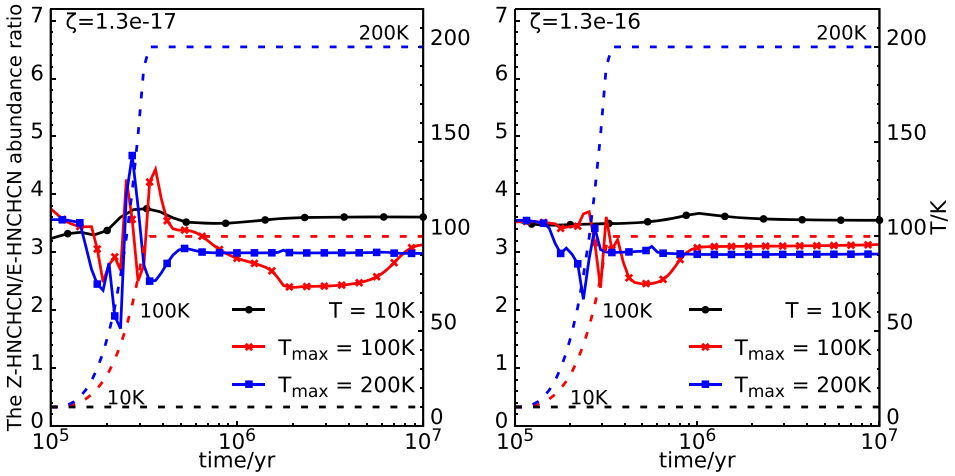

Figure 12. The calculated abundance ratio between the Z-isomer and the E-isomer in the gas phase over time with isothermal (black line with solid dots) and warm-up models (red line with crosses and blue line with solid squares). The left-hand panel corresponds to $\zeta = 1.3 \times 10^{-17}$ s^{-1}: black line corresponds to $n_{\rm H} = 2 \times 10^4$ cm^{-3}, $T = 10$ K; red line with crosses corresponds to $n_{\rm H} = 2 \times 10^5$ cm^{-3}, $T_{\rm max} = 100$ K; blue line with solid squares corresponds to $n_{\rm H} = 2 \times 10^6$ cm^{-3}, $T_{\rm max} = 200$ K. The right-hand panel's physical parameters are similar to those of the left-hand panel except for $\zeta = 1.3 \times 10^{-16}$ s^{-1}. The dashed lines correspond to temperature profiles.

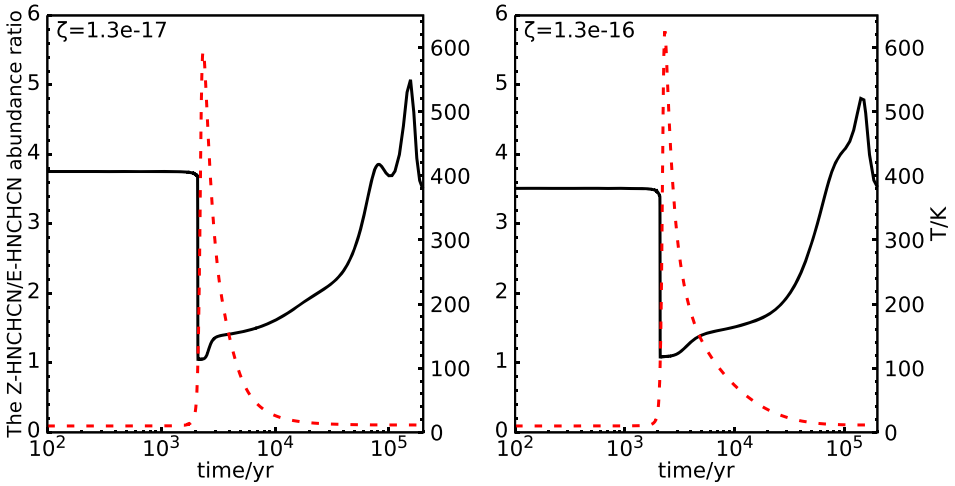

Figure 13. The calculated abundance ratio between the Z-isomer and the E-isomer in the gas phase over time with shock models. The left-hand panel corresponds to an evolutionary time of 3×10^5 yr using standard cold core conditions before shock onset, an initial temperature of 10 K, $n_{\rm H} = 2 \times 10^4$ cm^{-3}, and $\zeta = 1.3 \times 10^{-17}$ s^{-1}. The right-hand panel's physical parameters are similar to those of the left-hand panel except for the evolutionary time of 1×10^6 yr before the shock onset. The dashed lines correspond to temperature profiles.

scales of ∼1–2 × 10^5 and ∼1–5 × 10^5 yr, respectively, while the cold models cannot effectively produce the cyanomethanimine in the gas phase. The warm-up models terminating at lower temperatures, known as lukewarm models, with $T_{\rm max} = 30$ and 50 K, can produce more cyanomethanimine molecules in the granular phase compared with isothermal models. Once the grain is heated, via thermal warming in hot cores or shock heating, desorption will sooner or later occur from the grain surface.

In the C-type shock models, the results show reasonable agreement between the calculated cyanomethanimine abundances in comparison with the observed values in a time range of 10^4–10^5 yr. From the simulation, the gas-phase Z-/E-cyanomethanimine abundance ratios range 2–5 for isothermal and warm-up models and in the range of 1–5 for shock models, all of which generally agree with the observed value of ∼6 in the quiescent molecular cloud G+0.693 (Rivilla et al. 2019).

We conclude that the cyanomethanimine isomers are most likely to be formed within or near a hot core without the impact of shocks, or in the cold regions with shocks. The source Orion KL is a massive star formation region similar to Sgr B2(N), with high kinetic temperatures, as well as widespread shocks. Moreover, the precursor molecule CH_2NH exists toward Orion KL, so according to our simulations, Orion KL can be a candidate for detecting cyanomethanimine molecules.

ACKNOWLEDGEMENTS

This work was supported by the National Natural Science Foundation of China under grants 11973075, 11673054, and 11433008. EH wishes to acknowledge funding from the National Science Foundation (USA) through grant AST-1906489. The Taurus High Perfor-

mance Computing System of Xinjiang Astronomical Observatory was used for the simulations.

DATA AVAILABILITY

The data underlying this paper are available in the paper and in its online supplementary material.

REFERENCES

Anicich V. G., 2003, JPL Publication 03-19, NASA (http://hdl.handle.net/2014/7981)
Balucani N., Ceccarelli C., Taquet V., 2015, MNRAS, 449, L16
Becke A. D., 1993, J. Chem. Phys., 98, 5648
Belloche A., Menten K. M., Comito C., Müller H. S. P., Schilke P., Ott J., Thorwirth S., Hieret C., 2008, A&A, 482, 179
Belloche A., Müller H. S. P., Menten K. M., Schilke P., Comito C., 2013, A&A, 559, A47
Belloche A., Müller H. S. P., Garrod R. T., Menten K. M., 2016, A&A, 587, A91
Blake G. A., Sutton E. C., Masson C. R., Phillips T. G., 1987, ApJ, 315, 621
Bonfand M., Belloche A., Menten K. M., Garrod R. T., Müller H. S. P., 2017, A&A, 604, A60
Bonfand M., Belloche A., Garrod R. T., Menten K. M., Willis E., Stéphan G., Müller H. S. P., 2019, A&A, 628, A27
Borget F., Danger G., Duvernay F., Chomat M., Vinogradoff V., Theulé P., Chiavassa T., 2012, A&A, 541, A114
Brown R. D., Godfrey P. D., Ottrey A. L., Storey J. W. V., 1977, J. Mol. Spectrosc., 68, 359
Chakrabarti S., Chakrabarti S. K, 2000, A&A, 354, L6
Chengalur J. N., Kanekar N., 2003, A&A, 403, L43
Chuang K.-J., Fedoseev G., Ioppolo S., van Dishoeck E. F., Linnartz H., 2015, MNRAS, 455, 1702
Clemmnos J. H., Jasien P. G., Dykstra C. E., 1983, Mol. Phys., 48, 631
Crapsi A., Caselli P., Walmsley C. M., Myers P. C., Tafalla M., Lee C. W., Bourke T. L., 2005, ApJ, 619, 379
Crocker R. M., Jones D., Protheroe R. J., Ott J., Ekers R., Melia F., Stanev T., Green A., 2007, ApJ, 666, 934
Draine B. T., Salpeter E. E., 1979, ApJ, 231, 438
Enrique-Romero J., Rimola A., Ceccarelli C., Ugliengo P., Balucani N., Skouteris D., 2019, ACS Earth Space Chem., 3, 2158
Fedoseev G., Ioppolo S., Zhao D., Lamberts T., Linnartz H., 2015, MNRAS, 446, 439
Flower D. R., Pineau des Forêts G., 2015, A&A, 578, A63
Friberg P., 1984, A&A, 132, 265
Frisch M. J. et al., 2009, Gaussian 09, Revision B.01. Gaussian, Inc., Wallingford, CT
Garrod R. T., Herbst E., 2006, A&A, 457, 927
Garrod R. T., Wakelam V., Herbst E., 2007, A&A, 467, 1103
Garrod R. T., Widicus Weaver S. L., Herbst E., 2008, ApJ, 682, 283
Graedel T. E., Langer W. D., Frerking M. A., 1982, ApJS, 48, 321
Hasegawa T. I., Herbst E., 1993, MNRAS, 261, 83
Hasegawa T. I., Herbst E., Leung C. M., 1992, ApJS, 82, 167
Hasegawa T., Sato F., Whiteoak J. B., Miyawaki R., 1994, ApJ, 429, L77
Hassel G. E., Herbst E., Garrod R. T., 2008, ApJ, 681, 1385
Henshaw J. D. et al., 2016, MNRAS, 457, 2675
Holdship J. et al., 2016, MNRAS, 463, 802
Hollis J. M., Jewell P. R., Lovas F. J., Remijan A., 2004, ApJ, 613, L45
Hüttemeister S., Dahmen G., Mauersberger R., Henkel C., Wilson T. L., Martín-Pintado J., 1998, A&A, 334, 646
Jung S. H., Choe J. C., 2013, Astrobiology, 13, 465
Kelly G., Viti S., García-Burillo S., Fuente A., Usero A., Krips M., Neri R., 2017, A&A, 597, A11
Lee C., Yang W., Parr R. G., 1988, Phys. Rev. B, 37, 785
Lefloch B. et al., 2012, ApJ, 757, L25
Lis D. C., Goldsmith P. F., 1989, in Allamandola L. J., Tielens A. G. G. M., eds, Proc. IAU Symp. 135, Interstellar Dust. Springer, Netherlands, p. 205
Lis D. C., Goldsmith P. F., 1990, ApJ, 356, 195
Lis D. C., Goldsmith P. F., 1991, ApJ, 369, 157
Looney L. W., Mundy L. G., Welch W. J., 2000, ApJ, 529, 477
López-Sepulcre A. et al., 2015, MNRAS, 449, 2438
Maret S., Ceccarelli C., Caux E., Tielens A. G. G. M., Castets A., 2002, A&A, 395, 573
Martín S., Requena-Torres M. A., Martín-Pintado J., Mauersberger R., 2008, ApJ, 678, 245
Martín-Pintado J., de Vicente P., Wilson T. L., Johnston K. J., 1990, A&A, 236, 193
Martín-Pintado J., Gaume R. A., Rodríguez-Fernández N., de Vicente P., Wilson T. L., 1999, ApJ, 519, 667
Martín-Pintado J., Rizzo J. R., de Vicente P., Rodríguez-Fernández N. J., Fuente A., 2001, ApJ, 548, L65
Melosso M. et al., 2018, A&A, 609, A121
Motte F., Bontemps S., Louvet F., 2018, ARA&A, 56, 41
Neill J. L. et al., 2014, ApJ, 789, 8
Nummelin A., Bergman P., Hjalmarson Å., Friberg P., Irvine W. M., Millar T. J., Ohishi M., Saito S., 2000, ApJS, 128, 213
Öberg K. I., Fuchs G. W., Awad Z., Fraser H. J., Schlemmer S., van Dishoeck E. F., Linnartz H., 2007, ApJ, 662, L23
Ott J., Weiß A., Staveley-Smith L., Henkel C., Meier D. S., 2014, ApJ, 785, 55
Peng C., Schlegel H. B., 1993, Israel J. Chem., 33, 449
Petrie S. T., Millar J., Markwick A. J., 2003, MNRAS, 341, 609
Pineau des Forêts G., Roueff E., Schilke P., Flower D. R., 1993, MNRAS, 262, 915
Puzzarini C., 2015, J. Phys. Chem. A, 119, 11614
Quan D., Herbst E., 2007, A&A, 474, 521
Quan D., Herbst E., Osamura Y., Roueff E., 2010, ApJ, 725, 2101
Quan D., Herbst E., Corby J. F., Durr A., Hassel G., 2016, ApJ, 824, 129
Raksit A. B., Bohme D. K., 1984, Can. J. Chem., 62, 2123
Reboussin L., Wakelam V., Guilloteau S., Hersant F., 2014, MNRAS, 440, 3557
Requena-Torres M. A., Martín-Pintado J., Rodríguez-Franco A., Martín S., Rodríguez-Fernández N. J., de Vicente P., 2006, A&A, 455, 971
Rimola A., Skouteris D., Balucani N., Ceccarelli C., Enrique-Romero J., Taquet V., Ugliengo P., 2018, ACS Earth Space Chem., 2, 720
Rivilla V. M., Martín-Pintado J., Jiménez-Serra I., Zeng S., Martín S., 2019, MNRAS, 483, L114
Rodríguez-Fernández N. J., Tafalla M., Gueth F., Bachiller R., 2010, A&A, 516, A98
Ruaud M., Wakelam V., Hersant F., 2016, MNRAS, 459, 3756
Semenov D. et al., 2010, A&A, 522, A42
Smith I. W. M., Talbi D., Herbst E., 2001, A&A, 369, 611
Stutzki J., Genzel R., Graf U. U., Harris A. I., Jaffe D. T., 1989, ApJ, 340, L37
Takano S., Sugie M., Sugawara K.-I., Takeo H., Matsumura C., Masuda A., Kuchitsu K., 1990, J. Mol. Spectrosc., 141, 13
Theule P., Borget F., Mispelaer F., Danger G., Duvernay F., Guillemin J. C., Chiavassa T., 2011, A&A, 534, A64
Troland T. H., Heiles C., 1986, ApJ, 301, 339
Van der Tak F. F. S., Belloche A., Schilke P., Güsten R., Philipp S., Comito C., Bergman P., Nyman L.-Å., 2006, A&A, 454, L99
Vastel C., Loison J. C., Wakelam V., Lefloch B., 2019, A&A, 625, A91
Vazart F., Latouche C., Skouteris D., Balucani N., Barone V., 2015a, ApJ, 810, 111
Vazart F., Calderini D., Skouteris D., Latouche D., Barone. V., 2015b, J. Chem. Theory Comput., 11, 1165
Vidal T. H. G., Loison J.-C., Jaziri A. Y., Ruaud M., Gratier P., Wakelam V., 2017, MNRAS, 469, 435
Wakelam V., Herbst E., 2008, ApJ, 680, 371
Wakelam V. et al., 2010, Space Sci. Rev., 156, 13
Wakelam V. et al., 2012, ApJS, 199, 21

Wakelam V. et al., 2015, ApJS, 217, 20
Winnewisser M., Winnewisser B. P., Wentrup C., 1984, J. Mol. Spectrosc., 105, 193
Woon D. E., Herbst E., 2009, ApJS, 185, 273
Yim M. K., Choe J. C., 2012, Chem. Phys. Lett., 538, 24
Zaleski D. P. et al., 2013, ApJ, 765, L10

SUPPORTING INFORMATION

Supplementary data are available at *MNRAS* online.

Appendix A. Related reactions.
Table A1. Summary of the rate coefficients of gas-phase reactions involving Z-cyanomethanimine.
Table A2. Summary of the rate coefficients of surface reactions involving Z-cyanomethanimine.
Table A3. Summary of the rate coefficients of gas-phase reactions involving N-cyanomethanimine(CH_2NCN).
Table A4. Summary of the rate coefficients of surface reactions involving N-cyanomethanimine(CH_2NCN).
Table A5. Summary of the rate coefficients of gas-phase reactions involving other species.
Table A6. Summary of the rate coefficients of surface reactions involving other species.

Please note: Oxford University Press is not responsible for the content or functionality of any supporting materials supplied by the authors. Any queries (other than missing material) should be directed to the corresponding author for the article.

This paper has been typeset from a TEX/LATEX file prepared by the author.